

PULSE PROFILES, SPECTRA AND POLARIZATION CHARACTERISTICS OF NON-THERMAL EMISSIONS FROM THE CRAB-LIKE PULSARS

J.Takata

*Institute of Astronomy and Astrophysics, Academia Sinica; and Theoretical Institute for
Advanced Research in Astrophysics, Academia Sinica and National Tsing Hua University,
Taipei Taiwan*

and

H.-K.Chang

*Department of Physics and Institute of Astronomy, National Tsing Hua University,
Hsinchu, Taiwan*

ABSTRACT

We discuss non-thermal emission mechanism of the Crab-like pulsars with both a two-dimensional electro-dynamical study and a three-dimensional model. We investigate the emission process in the outer gap accelerator. In the two-dimensional electro-dynamical study, we solve the Poisson equation of the accelerating electric field in the outer gap and the equation of motion of the primary particles with the synchrotron and the curvature radiation process and the pair-creation process. We show a solved gap structure which produces a consistent gamma-ray spectrum with EGRET observation. Based on the two-dimensional model, we conduct a three-dimensional emission model to calculate the synchrotron and the inverse-Compton processes of the secondary pairs produced outside the outer gap. We calculate the pulse profiles, the phase-resolved spectra and the polarization characteristics in optical to γ -ray bands to compare the observation of the Crab pulsar and PSR B0540-69. For the Crab pulsar, we find that the outer gap geometry extending from near the stellar surface to near the light cylinder produces a complex morphology change of the pulse profiles as a function of the photon energy. This predicted morphology change is quite similar with that of the observations. The calculated phase-resolved spectra are consistent with the data through optical to the γ -ray bands. We demonstrate that

the 10~20 % of the polarization degree in the optical emissions from the Crab pulsar and the Vela pulsar are explained by the synchrotron emissions with the particle gyration motion. For PSR B0540-69, the observed pulse profile with a single broad pulse is reproduced with a thicker emission region and a smaller inclination angle between the rotational axis and the magnetic axis than the Crab pulsar.

Subject headings: optical- X ray-gamma rays:theory-pulsars:Crab like -radiation mechanisms:non-thermal

1. Introduction

The observed strong γ -ray emissions from the seven young pulsars (Thompson 2003) show that electrons and positrons are accelerated up to ultra-relativistic regime in the pulsar magnetosphere. The Crab pulsar (PSR B0531+21), which is one of the brightest and the youngest γ -ray emitting pulsar, shows the non-thermal emission properties in optical to γ -ray bands. The observed spectrum of the pulsed photons emitted from the Crab pulsar extends continuously from optical to γ -ray bands with the spectral index α_ν , defined as $I_\nu \propto \nu^{-\alpha_\nu}$, varying from $\alpha_\nu \sim 0$ in optical wavelengths, $\alpha_\nu \sim 0.5$ in X -ray bands, to $\alpha_\nu \sim 2$ in γ -ray bands. The pulse profile has two peaks in a single period, and the positions of the pulse peaks across the wide energy range are approximately all in phase (Kuiper et al. 2001). Interestingly, the pulse profile morphology changes significantly as a function of the photon energy. The first peak (denoted Peak 1 in the following) dominates in optical wavelengths. However, the second peak (Peak 2) becomes more and more pronounced for increasing energies and eventually the Peak 2 emission dominates in soft γ -ray bands. Above 10 MeV photon energy, Peak 1 again dominates Peak 2. The electromagnetic spectrum of the non-thermal emissions also changes with pulse phases. In the future, the phase-resolved spectra above 10 MeV will be measured with a sensitivity better than that of the Energetic Gamma-Ray Experiment Telescope on board the *Compton Gamma-ray Observatory* by, for example, GLAST LAT. These observed detail properties for the pulse profiles and the phase-resolved spectra will be useful to discriminate the proposed emission models.

In addition to the pulse profiles, Kanbach et al.(2005) measured the polarization characteristics of the pulsed photons from the Crab pulsar in the optical wavelengths. The observation revealed that the degree of the polarization at each pulse peak is lower than 10 % and a large swing of the position angle of the electric-vector of the radiation appears at each pulse peak. The polarization measurements provide two additional observed properties, namely, the degree and the position angle of the polarization. In the future, the polarization

of X -ray and soft γ -ray emissions from the pulsar will probably be able to be measured by ongoing projects such as PoGO (Kataoka et al. 2005) and NCT (Chang et al. 2007) projects. Therefore, a theoretical study, particularly on the polarization characteristics, is not only desired, but also timely for the understanding the non-thermal emission process in the pulsar magnetospheres.

The polar cap accelerator (Ruderman and Sutherland 1975; Daugherty and Harding 1996) and the outer magnetospheric accelerator, the so called outer gap model (Cheng et al. 1986a,b; Romani 1996), were proposed as the possible acceleration sites in the pulsar magnetospheres. The traditional polar cap model assumes an acceleration region expanding several stellar radii from the stellar surface around the magnetic pole. On the other hand, the traditional outer gap assumes an acceleration region extending beyond the null surface of the Goldreich-Julian charge density at the outer magnetosphere. The Goldreich-Julian charge density is given by $\rho_{GJ} \sim -\boldsymbol{\Omega} \cdot \mathbf{B}/2\pi c$ (Goldreich and Julian 1969) with $\boldsymbol{\Omega}$ being the rotational frequency of the star, \mathbf{B} the magnetic field, and c the speed of light. Both models assume the particle acceleration by an electric field parallel to the magnetic field line. In the pulsar magnetosphere, the accelerating electric field arises in the region where the local charge density differs from the Goldreich-Julian charge density.

The slot gap model (Muslimov & Harding 2004), which is an extended polar cap model, predicts that the acceleration region extends up to near the light cylinder around the last-open field lines because the pair-formation front, which screens the accelerating electric field, occurs at higher altitude around there. Two-dimensional electro-dynamical studies (Takata et al. 2004, 2006; Hirotani 2006) suggested that the inner boundary of the outer gap locates near (or at) the stellar surface because of the current through the outer gap. Although the recent polar-slot gap and outer gap models both predict similar geometry of the acceleration region, an important difference between the two models is the electric field configuration in the accelerator. For the slot gap accelerator, the electric field is stronger nearer the stellar surface and smaller at higher altitude. On the other hand, the outer gap model predicts a stronger electric field beyond the null surface and a smaller one below the null surface due to the screening effect of electron and positron pairs. This difference in the electric field configuration, and the resultant difference in the acceleration and the emission structures will appear as a difference in the predicted pulse profiles, the phase-resolved spectra and the polarization characteristics, which can be examined by a three-dimensional model.

Within the framework of the traditional outer gap model, Romani & Yadigaroglu (1995) considered a three-dimensional geometry and explained the general features of the observed pulse profile such as two-peaks in a single period. Subsequently, Cheng et al. (2000, hereafter CRZ00) developed the three-dimensional outer gap model, in which the gap is sustained

self-consistently by the pair-creation process between the primary photons emitted via the curvature process and the surface X -ray photons. CRZ00 calculated the phase-resolved spectrum in γ -ray region for the Crab pulsar with the synchrotron radiation and the inverse Compton scattering of the electron and positron pairs produced outside the gap. Zhang & Cheng (2002) reconsidered the CRZ00 model to examine the phase-resolved spectra in X -ray region. However, it has been difficult to explain the detail features of the observed pulse profiles and phase-resolved spectra with the traditional model. Furthermore, the previous studies have not discussed the complex features of the observed pulse profiles from optical to γ -ray bands. Recently, Takata et al. (2007) explained the observed polarization characteristics in the optical wavelengths (Kanbach et al 2005) with the new outer gap geometry. Jia et al. (2007) examined the phase-resolved spectra by taking account of the emissions below null charge surface. However, these studies also did not consider the pulse profile, the phase-resolved spectra and the polarization characteristics in optical to γ -ray bands, simultaneously.

In this paper, we study the emission process of the Crab-like pulsars with the outer gap accelerator model from both a two-dimensional electro-dynamical model and a three-dimensional emission model point of views. In first part (section 2) of this paper, we will summarize the results of the two-dimensional electro-dynamical study, in which the outer gap structure for the Crab pulsar is solved with the Poisson equation, the particle motion, the radiation process and the pair-creation process in meridional plane, following Takata et al (2004, 2006) and Hiro-tani (2006). We will show a result which has a consistent GeV spectrum with the observed phase-averaged spectrum of the Crab pulsar. In the second part (sections 3 and 4), we will conduct a three-dimensional outer gap model based on the results of the two-dimensional electro-dynamical study. In the three-dimensional study, the main purpose is to discuss the emission process of optical to γ -ray photons by examining the morphology change of the pulse profile as a function of the photon energy and the phase-resolved spectra for the Crab pulsar with the outer gap accelerator model. We will predict the polarization characteristics through optical to γ -ray bands. We also apply the model to a Crab-like pulsar, PSR B0540-69. The Crab pulsar and PSR B0540-69 are sometimes called twin pulsars, because their pulsar parameters are very similar to each other. However, the observed shapes of pulse profiles are very different to each other. This pair will give an unique opportunity to examine the model capability.

Important differences between present and previous three-dimensional studies are as follows. First, we take into account the emissions both below and beyond the null surface as the electro-dynamical study has predicted, while only the emissions beyond the null surface were taken into account in CRZ00. Secondary we discuss the morphology change of the pules profile by calculating local emissivity as a function of the photon energy, while the

previous studies did not discuss the morphology change because they assumed a constant emissivity when the pulse profiles were calculated. We deal the gyration motion of the pairs because the gyration motion causes the depolarization for the synchrotron radiation. We adopt the rotating dipole field in the observer frame, while the previous studies adopted it in the co-rotating frame. Though these effects were considered in Takata et al. (2007), they calculated only the synchrotron emission process and presented the phase-averaged spectrum below MeV energy. In this paper, we extend the model spectrum up to γ -ray bands by computing also the inverse Compton scattering. Finally, we calculate the collision angle of the inverse Compton scattering between the pairs and the background synchrotron photons by tracing the three-dimensional trajectory of the synchrotron photons, while the isotropic distribution of the back ground photons was assumed in the previous studies (CRZ00). The collision angle greatly affects to the emissivity of and the polarization characteristics of the inverse Compton scattering. By including all these effects, we examine the pulse profiles, the phase-resolved spectra and the polarization characteristics in optical to γ -ray bands, simultaneously.

2. Results of Two-dimensional Electrodynamical Model

In this section, we summarize the results of the two-dimensional electrodynamic study for the Crab pulsar. Following Takata et al (2004, 2006) and Hirovani (2006) we calculate the spectrum of the synchrotron and curvature radiation processes of the primary particles with the electric structure by solving the Poisson equation [$\nabla^2\Phi = -4\pi(\rho - \rho_{GJ})$], the equation of motion for the particles, the pair-creation process and the radiation process. As discussed in Takata et al. (2004, 2006), the electric structure depends on the current and the gap size, which are model parameters in their studies. In this section, we show a result, which produces a consistent GeV spectrum with the observations. We ignore the effect of the gravity which is not important for the dynamics of the outer gap accelerator. We adopt static dipole field, while in the later section of the three-dimensional study, we apply the rotating dipole field. The obtained electric structure with the static and the rotating dipole field did not change very much, because the radial distances to the null charge points, that is, to the gap position are similar to each other. For the pair-creation process in the gap, we consider the thermal soft-photons coming from the stellar surface. We adopt $kT = 170$ eV for the Crab pulsar (Yakovlev & Pethick 2004). The inclination angle is assumed as $\alpha = 50^\circ$.

Thick solid line in Figure 1 shows the solved accelerating electric field along the field line locating at 50 % of the trans-field thickness from the lower boundary (last-open field line). Here, we assume $0.1R_{lc}$ of the gap thickness at the light cylinder and the outer boundary is

puted at near the light cylinder. We also assume that 5% of the Goldreich-Julian current, $0.05\Omega B/2\pi$, is injected at the outer boundary.

The position of the inner boundary is solved with the current, for which about 22 % of the Goldreich-Julian current runs through the outer gap in the present case. From Figure 1, we can see that the inner boundary ($r \sim 0.18R_{lc}$) is inside of the null charge point ($r \sim 0.29R_{lc}$). As suggested by Takata et al. (2004), the inner boundary is located at the position, on which $j_g + j_2 - j_1 \sim B_z/B$ is satisfied, where j_g is non-dimensional current created in the gap, j_1 and j_2 are non-dimensional current injected at the inner and the outer boundaries, respectively. For example, for no injection currents, $j_1 = j_2 = 0$, the inner boundary is located at the null charge surface, where $B_z = 0$, if no current is created inside of the gap ($j_g = 0$) as the vacuum case. On the other hands, if $j_g \sim \cos \alpha$, where α is the inclination angle, is created, the inner boundary is located at the stellar surface on which $B_z/B \sim \cos \alpha$ is satisfied around the magnetic pole. In the present case, the inner boundary is located at the position of about 65 % of the radial distance to the null point with the current components $(j_g, j_1, j_2) = (0.17, 0, 0.05)$.

Figure 2 shows the calculated synchrotron-curvature spectrum and compares with the observed phase-averaged spectrum. Solid-line shows spectrum of the intrinsic radiation from the outer gap, while the dashed-line represents the appearance spectrum after attenuation of the photons via pair-creation process outside of the gap with the soft photon-field emitted by the synchrotron process of the secondary pairs. We calculate the initial pitch angle of the pairs from the propagating direction of the curvature photons and the magnetic field direction at the pair-creation position. For obtaining the luminosity, we assume the gap opening angle ~ 250 degree in the azimuthal direction (see section 3.1).

As dashed-line shows the large amount of the curvature photons above 500 MeV are converted into the secondary pairs outside of the gap via the pair creation process with the X-ray photons from the secondary pairs. We find from Figure 2 that the shape of the spectral energy distribution after absorption becomes relatively flat and explains the observation above 100 MeV.

The inverse-Compton process of the primary particles in the gap is a possible mechanism for TeV emissions. However, the present model predicts the TeV flux for the Crab pulsar is too low to detect the present Cherenkov telescopes. The soft-photons emitted by secondary pairs above the gap may not be able to illuminate the gap due to the curvature of the field lines, and only thermal photons from the stellar surface may be scattered by the primary particles. In such a case, we found that the intrinsic flux on the Earth becomes $\sim 10^{-15}$ erg/cm²s, which is much small compared with the sensitivity of the present Cherenkov telescope. On the other hand, some soft-photons emitted by secondary pairs may

illuminate the outer gap because of the effects of the pitch angle. In such a case, we obtained intrinsic TeV flux which is easily detected by present instruments. However, the optical depth of the pair-creation for TeV photons is much larger than unity in the magnetosphere, and the residual TeV photons are a very few, which is difficult to detect with the present instruments.

From Figure 2, we can see that the synchrotron and curvature radiations of the primary particles in the outer-gap does not explain the observed flux below 100 MeV. We consider that the secondary pairs created outside gap produce below 100 MeV photons via the synchrotron and the inverse-Compton process. Furthermore, the present two-dimensional model can compare with only the phase-averaged spectrum. More detailed observation such like the pulse profile, the phase-resolved spectra and the polarization require a three-dimensional model. Following sections, therefore, we calculate the emission process of the secondary pairs and conduct a three-dimensional model.

3. A Three-Dimensional Emission Model

In the following, we conduct a three-dimensional emission model. We anticipate that the emission direction is coincide with the particle motion in the observer frame. In the present paper, we adopt the rotating dipole field in the observer frame while it was assumed in the co-rotating frame in the previous studies (Romani & Yadigaroglu 1995; Cheng et al 2000; Dyks et al 2004). As a results, the magnetic field configurations and resultant the morphology of emission pattern in the observer frame are different between the present and the previous studies, but the difference becomes to be important only near the light cylinder. In the present study, furthermore, we discuss the model in the observer frame only, and we do not introduce the co-rotating frame.

3.1. Electric field

We have to describe the accelerating electric field into the three-dimensional from. Based on the result (Figure 1) of the two-dimensional electro-dynamical study, we adopt the following three-dimensional form. First, we use the vacuum solution obtained by Cheng et al. (1986a),

$$E_{\parallel}(r) = \frac{\Omega B(r) f^2(r) R_{lc}^2}{cs(r)}, \quad (1)$$

beyond the null charge surface, where $s(r)$ is the curvature radius of the magnetic field line and $f(r)$ is the fractional gap thickness. We can calculate the electric field at each point

having a three-dimensional radial distance, r . Below null surface, we assume 50 % of the strength of the electric field at the null point given by equation (1). The dashed-line in Figure 1 shows the electric field strength of the approximation form in the meridional plane. We can see that the typical strength of the electric field by the two-dimensional electro-dynamical study (solid-line) in the meridional plane is in general described by the present simple form (dashed-line). In fact, as long as the gap is geometrically thin in the trans-field direction and the magnitude of the current is smaller than the Goldreich-Julian value, the vacuum solution beyond the null charge surface approximately describes the typical strength of the accelerating field in the meridional plane. Now, we assume that this simple form can describe also the typical strength of the three-dimensional distribution of the accelerating electric field.

At each point, the maximum Lorentz factor of the particles are determined by the force balance between the acceleration by the electric and curvature radiation back reaction, $\Gamma_p(r) = [3s^2(r)E_{||}/2e]^{1/4}$, where $\Omega_2 = \Omega/100s^{-1}$. The primary particle emits high-energy photons as the curvature radiation process, whose typical energy is $E_{curv}(r) = 3h\Gamma_p^3(r)c/4\pi s(r)$, and the local power of the curvature radiation is given by $l_{curv} = eE_{||}c$.

It is important to estimate the polar cap opening angle of the active region of the outer gap accelerator. When we consider an open-field line through the outer gap, the pair-creation process between the primary curvature photons and the surface X -rays mainly occurs near and below the null charge surface. Therefore, we may be able to relate the opening angle with the pair-creation mean free path, which is estimated as $l(r) \sim [2s(r)f(r)R_{lc}] \sim 2f^{1/2}(R_{lc}/2)r$, at the null surface. In the present paper, we constrain the width of the polar cap angle of the active gap by the condition that the mean-free path at the null charge point on the magnetic field line becomes shorter than the light radius. This condition produces the width of the polar cap angle of $\sim 250^\circ$.

3.2. Distribution and motion of the secondary pairs

As we demonstrated in section 2, a significant amount of the curvature photons above ~ 500 MeV convert into secondary pairs outside the gap via the photon-photon pair-creation process with the soft-photons emitted by the synchrotron radiation of the secondary pairs. From Figure 2, furthermore, we can read that the spectrum of the intrinsic emissions has the photon index of about -1 . Therefore, we may approximately describe the local curvature spectrum with $F_{curv} \sim l_{curv}jn_{GJ}/E_{curv}E_\gamma$, where j represent the current in units of the Goldreich-Julian value. Using the steady loss equation, $d[\dot{E}_e dn/dE_e]/dE_e = Q(E_e)$, we

obtain the distribution of the secondary pairs as

$$\frac{dn_e}{dE_e} \sim \begin{cases} l_{curv} j n_{GJ} \ln(E_{curv}/2E_e) / \dot{E}_e E_{curv} & \text{for } 500 \text{ MeV} < 2E_e < E_{curv} \\ l_{curv} j n_{GJ} \ln(E_{curv}/500 \text{ MeV}) / \dot{E}_e E_{curv} & \text{for } 2E_e < 500 \text{ MeV} \end{cases} \quad (2)$$

where $\dot{E}_e = 2e^4 B^2(r) \sin^2 \theta_p(r) \Gamma_e^2 / 3m_e^2 c^3$ is the energy loss rate of the synchrotron radiation of the secondary pairs, θ_p is the pitch angle, and Γ_e is the Lorentz factor of the pairs. The local pitch angle will be expressed as $\sin \theta_p(r) \propto \sqrt{2f(r)R_L/s(r)}$. Because $f(r) = f(R_{lc})(r/R_{lc})^{3/2}$ and $s(r) \sim \sqrt{rR_{lc}}$ are satisfied for the dipole field, we may relate with $\sin \theta_p(r) = (r/R_{lc})^{1/2} \sin \theta_p(R_{lc})$ between the pitch angle of the local point and the light cylinder along the field lines. Outside the gap, the pairs lose most of their energy via the synchrotron process. Because the synchrotron loss rate \dot{E}_e is proportional to square of the particle energy, the power law index of the distribution given by equation (2) becomes $p \sim 2$, which produces a synchrotron spectrum with the spectral index of $\alpha_\nu \sim 0.5$.

In the observer frame, we may describe the particle motion outside the gap with

$$\boldsymbol{\beta} = \beta_0 \cos \theta_p \mathbf{b} + \beta_0 \sin \theta_p \mathbf{b}_\perp + \beta_{co} \mathbf{e}_\phi, \quad (3)$$

where the first term and the second term in the right hand side represent, respectively, the particle motion parallel to the magnetic field and gyration motion, and the third term represents the co-rotational motion with the non-dimensional velocity $\beta_{co} = \varpi/R_{lc}$, where ϖ is the axial distance. The vector \mathbf{b} is the unit vector along the field line and \mathbf{b}_\perp represents the unit vector perpendicular to the magnetic field line, $\mathbf{b}_\perp \equiv \pm(\cos \delta\phi \mathbf{K} + \sin \delta\phi \mathbf{K} \times \mathbf{b})$, where the sign + (or –) corresponds to gyration of the positrons (or electrons), $\mathbf{K} = (\mathbf{b} \cdot \nabla) \mathbf{b} / |(\mathbf{b} \cdot \nabla) \mathbf{b}|$ is the unit vector of the curvature of the magnetic field line, and $\delta\phi$ represents the phase of gyration around the magnetic field. Because the pairs have an ultra-relativistic speed, we determine the value of the coefficient β_0 from the condition that $|\boldsymbol{\beta}| = 1$. We anticipate that the photons are emitted in the direction of the particle motion of equation (3).

We note that the synchrotron radiation after collecting of the photons is greatly depolarized due to the gyration motion of the pairs, although the intrinsic radiation is highly polarized. Therefore, the observed small polarization degree $\sim 10\%$ at the optical bands for not only the Crab pulsar, but also for the Vela pulsar (Mignami et al. 2007) are easily reproduced by the synchrotron emission model (Takata et al. 2007).

We assume that the emission region of the secondary pairs extends just above the outer gap with thickness of the mean free path of the pair-creation $\lambda \sim 10^7 \text{ cm} \sim 0.1 R_{lc}$ for the Crab pulsar. Some secondary high-energy photons via the inverse Compton scattering may convert into the tertiary pairs. The tertiary pairs will be produced above the emission region

of the secondary pairs, and its initial Lorentz factor will be smaller than that of the secondary pairs. We also take into account the effects of the emissions from the tertiary pairs.

3.3. Emission process of the secondary pairs and polarization

We consider that the synchrotron radiation and the inverse Compton scattering of the secondary pairs are major emission mechanisms for the observed non-thermal radiation through optical to γ -ray bands for the Crab-like pulsars. If we estimate the radiation powers of the synchrotron radiation and the inverse Compton scattering, we obtain

$$\frac{P_{syn}}{P_{IC}} \sim 10 \left(\frac{U_{ph}}{5 \cdot 10^7 \text{erg/cm}^3} \right)^{-1} \left(\frac{B}{10^6 \text{Gauss}} \right)^2 \left(\frac{\sin \theta_p}{0.1} \right)^2 \quad (4)$$

with U_{ph} being the energy density of the synchrotron photons. The estimated value will explain the observed flux ratio of 1 MeV and 100 MeV emissions of the Crab pulsar. We calculate only the outward emissions, because the inward emissions are expected to be much fainter than the outward emissions.

In the calculation, we firstly compute the volume emissivity of the synchrotron radiation and its emitting direction for each radiating point (section 3.3.1). Then, we trace the propagation of the synchrotron beam to simulate the scattering process by the pairs (section 3.3.2). On each scattering point, we calculate the volume emissivity and the polarization of the inverse Compton scattering for a specific viewing angle of the observer. We perform this procedure for all calculation points to obtain the total radiation for the specific observer. This procedure is equivalent with computing the radiation transfer,

$$\frac{dI(\mathbf{k}_1, \epsilon_1)}{ds} = j_s(\mathbf{k}_1, \epsilon_1) + j_i(\mathbf{k}_1, \epsilon_1), \quad (5)$$

where $I(\mathbf{k}_1, \epsilon_1)$ is the total intensity of the beam propagating in the direction of \mathbf{k}_1 , ϵ_1 is the energy of photons in units of the electron rest mass energy, $j_s(\mathbf{k}_1, \epsilon_1)$ is the volume emissivity of the synchrotron radiation, and $j_i(\mathbf{k}_1, \epsilon_1)$ represents the amount of the scattered photons into the direction \mathbf{k}_1 and to the energy ϵ_1 . We neglect the effects of the absorption, because the synchrotron self-absorption is not important above optical photon energy, where we are now interested in. Also, we ignore the effects of the scattering off from the direction \mathbf{k}_1 of the synchrotron photons, because the scattered photons are tiny amounts of total number of the synchrotron photons.

3.3.1. Synchrotron radiation

Assuming that all the synchrotron photons are radiated toward the particle motion direction, $\mathbf{k}_1 = \boldsymbol{\beta}$, the volume emissivity of the synchrotron radiation is calculated from

$$j_s(\epsilon_1) \equiv \frac{dI_s}{ds} = \frac{\epsilon_1 F_{syn}(\epsilon_1)}{\delta\Omega}, \quad (6)$$

where $\delta\Omega$ is the solid angle of the radiation, and F_{syn} is the photon spectrum described by

$$F_{syn}(\epsilon_1) = \frac{3^{1/2} e^3 B(r) \sin \theta_p(r)}{mc^2 h \epsilon_1} \int \left[\frac{dn_e(r)}{dE_e} \right] F(\epsilon_1/\epsilon_{syn}) dE_e, \quad (7)$$

where $\epsilon_{syn}(r) = 3he\Gamma_e^2(r)B(r)\sin\theta_p(r)/4\pi m_e^2 c^3$ is the typical photon energy of the pairs in units of the electron rest mass energy, Γ_e represents the Lorentz factor of the secondary pairs and $F(x) = x \int_x^\infty K_{5/3}(y) dy$ with $K_{5/3}$ being the modified Bessel function of order 5/3.

When we calculate the polarization of the synchrotron radiation, we anticipate that direction of the electric vector of the electro-magnetic wave propagating toward the observer is parallel to the projected direction of the acceleration of the particle on the sky, $\mathbf{E}_{em} \propto \mathbf{a} - (\mathbf{k}_1 \cdot \mathbf{a}) \mathbf{k}_1$, (Blaskiewicz et al. 1991), where the acceleration vector \mathbf{a} derived from equation (3) is approximately written by $\mathbf{a} \sim \pm \beta_0 \omega_B \sin \theta_p (-\sin \delta\phi \mathbf{K} + \cos \delta\phi \mathbf{K} \times \mathbf{b})$, where ω_B is the gyration frequency. We assume that the radiation at each point is linearly polarized with degree of $\Pi_{syn} = (p + 1)/(p + 7/2)$, where p is the power law index of the particle distribution. Because the observed radiation is consist of the radiations from the different particles with the different pitch angle, we assume that the circular polarization will cancel out and become zero in the observed radiation. The Stokes parameters Q_{syn} and U_{syn} are, respectively, calculated from $dQ_{syn}(\mathbf{k}_1, \epsilon_1)/ds = j_s(\mathbf{k}_1, \epsilon_1) \cos 2\eta_s(r)$ and $dU_{syn}(\mathbf{k}_1, \epsilon_1)/ds = j_s(\mathbf{k}_1, \epsilon_1) \sin 2\eta_s(r)$, where $\eta_s(r)$ is the position angle defined by the angle between the electric vector of the wave and the projected direction of the rotation axis on the sky, $\boldsymbol{\Omega}_p = \boldsymbol{\Omega} - (\mathbf{k}_1 \cdot \boldsymbol{\Omega}) \mathbf{k}_1$.

3.3.2. Inverse Compton scattering

To simulate the scattering process, we trace the three-dimensional trajectory of the synchrotron photons. When we trace the trajectory of the synchrotron photons, we define the Cartesian coordinate such that z -axis is along the rotation axis and the x -axis is in the meridional plane. By ignoring bending of the trajectory due to the gravity, the position of the photons after traveling distance δs is $x(\delta s) = (x_0 + k_{x_0} \delta s) \cos(\delta s/R_{lc}) + (y_0 + k_{y_0} \delta s) \sin(\delta s/R_{lc})$, $y(\delta s) = -(x_0 + k_{x_0} \delta s) \sin(\delta s/R_{lc}) + (y_0 + k_{y_0} \delta s) \cos(\delta s/R_{lc})$ and $z(\delta s) = z_0 + k_{z_0} \delta s$, where the

coordinates (x_0, y_0, z_0) are the radiating point of the synchrotron photon, and $(k_{x_0}, k_{y_0}, k_{z_0})$ represents the emission direction at (x_0, y_0, z_0) . The emission direction of the background synchrotron radiation is calculated from equation 3, which takes account the aberration due to the corotating motion.

Because the mean free path of a synchrotron photon of the scattering is much longer than the light radius, one can consider that the scattering rate is constant along the path of the synchrotron photons in the magnetosphere as the first order approximation. We determine the scattering points at regular interval, which is much shorter than the gap size, along the path of the synchrotron photons. In the calculation, we first compute the Stokes parameter of the Compton process in the electron rest frame, and then we transform it to the observer frame. In the following, the prime and 'non'-prime quantities represent the quantities in the electron rest frame and the observer frame, respectively. A detail derivation of equations of the Stokes parameters (8) and (10) are seen in Appendix A.

We denote the specific intensity of the synchrotron radiation propagating to the direction \mathbf{k}_0 in the observer frame with $I_0(\mathbf{k}_0, \epsilon_0)$, where ϵ_0 represents the energy of the background photons in units of the electron rest mass energy. In the electron rest frame, the background radiation becomes $I'_0(\mathbf{k}'_0, \epsilon'_0) = D_1^3 I_0(\mathbf{k}_0, \epsilon_0)$, where $D_1 = \epsilon'_0/\epsilon_0 = \Gamma_e^{-1}(1 + \beta \cos \theta'_0)$ is a Doppler factor, β is the velocity of the scattering particles in units of the speed of light, and $\Gamma_e = 1/\sqrt{1 - \beta^2}$. The polar angle θ_0 is defined by the angle between the directions of the particle motion and of the propagation of the background radiation, which becomes $\theta_0 \sim 0.1 - 0.3$ radian in numerically. For the particles with the Lorentz factor $10^3 \sim 10^4$, optical to X-ray photons are mainly scattered. In this photon energy bands, the synchrotron photons are distributed with a spectral index of $\alpha_\nu \sim 0.5$ because the cut-off energy of the synchrotron spectrum is ~ 1 MeV and because the particles are distributed with the index $p \sim 2$ (section 3.2). Because the synchrotron beam from each position is strongly collimated, we approximately describe the background beam, in which the center of the beam is direct to the polar angle θ_0 measured from the electron motion direction and the azimuthal direction ϕ_0 , as $I_0(\mathbf{k}_0, \epsilon) = C_0 \epsilon^{-0.5} \delta(\theta - \theta_0) \delta(\phi - \phi_0)$, where C_0 is evaluated from equation (6).

We are interested in the inverse Compton scattering with the background synchrotron radiation, which is partially polarized with $\Pi_{syn} \sim 70\%$. With unpolarized components of the background radiation propagating to the direction \mathbf{k}_0 , the volume emissivity j_u and the Stoke parameter Q_u and U_u of the scattered radiation propagating to the direction \mathbf{k}_1 are calculated from (see appendix A)

$$\left. \begin{aligned} j_u(\mathbf{k}_1, \epsilon_1) &\equiv dI_u(\mathbf{k}_1, \epsilon_1)/ds \\ dQ_u(\mathbf{k}_1, \epsilon_1)/ds \\ dU_u(\mathbf{k}_1, \epsilon_1)/ds \end{aligned} \right\} = (1 - \Pi_{syn}) \frac{3\sigma_T}{16\pi} C_0 \int d\Gamma_e \left[\frac{dn_e}{d\Gamma_e} \right]$$

$$\times \frac{\epsilon_0'^{-a}}{\Gamma_e^{4+a}(1 - \beta \cos \theta_1)^2(1 + \beta \cos \theta_0')^{a+1}} \left(\frac{\epsilon_1'}{\epsilon_0'}\right)^2 \begin{cases} \left[\frac{\epsilon_0'}{\epsilon_1'} + \frac{\epsilon_1'}{\epsilon_0'} - \sin^2 w_s'\right], \\ q_u' \cos 2\zeta - u_u' \sin 2\zeta, \\ q_u' \sin 2\zeta + u_u' \cos 2\zeta, \end{cases} \quad (8)$$

and

$$\begin{aligned} q_u' &= \sin^2 w_s' \cos 2\eta', \\ u_u' &= \sin^2 w_s' \sin 2\eta', \end{aligned} \quad (9)$$

where the Stokes parameters are measured from the rotation axis of the pulsar projected on the sky, and ζ is defined by the angle between the directions of the rotation axis and the particle motion projected on the sky (Figures 11). The polar angle θ_1 represents the propagating direction of the scattered photons measured from the particle motion direction, w_s is the scattering angle defined by $\cos w_s = \mathbf{k}_0 \cdot \mathbf{k}_1$ and the azimuthal angle η is the angle between the orthogonal direction to the scattering plane and the direction of the particle motion projected on the sky.

For the polarized component of the background radiation, the volume emissivity and the Stokes parameters are calculated from

$$\left. \begin{aligned} j_p(\mathbf{k}_1, \epsilon_1) &\equiv dI_p(\mathbf{k}_1, \epsilon_1)/ds \\ dQ_p(\mathbf{k}_1, \epsilon_1)/ds \\ dU_p(\mathbf{k}_1, \epsilon_1)/ds \end{aligned} \right\} = \Pi_{syn} \frac{3\sigma_T}{16\pi} C_0 \int d\Gamma_e \left[\frac{dn_e}{d\Gamma_e} \right]$$

$$\times \frac{\epsilon_0'^{-a}}{\Gamma_e^{4+a}(1 - \beta \cos \theta_1)^2(1 + \beta \cos \theta_0')^{a+1}} \left(\frac{\epsilon_1'}{\epsilon_0'}\right)^2 \begin{cases} \left[\frac{\epsilon_0'}{\epsilon_1'} + \frac{\epsilon_1'}{\epsilon_0'} - \sin^2 w_s' \cos^2 \lambda_p'\right], \\ q_p' \cos 2\zeta - u_p' \sin 2\zeta \\ q_p' \sin 2\zeta + u_p' \cos 2\zeta, \end{cases} \quad (10)$$

and

$$\begin{aligned} q_p' &= [\sin^2 w_s' - (1 + \cos^2 w_s') \cos 2\lambda_p'] \cos 2\eta' - 2 \cos w_s' \sin 2\lambda_p' \sin 2\eta', \\ u_p' &= [\sin^2 w_s' - (1 + \cos^2 w_s') \cos 2\lambda_p'] \sin 2\eta' - 2 \cos w_s' \sin 2\lambda_p' \cos 2\eta', \end{aligned} \quad (11)$$

where λ_p is the angle between the polarization plane of the background radiation and the plane of the scattering. By exploring the additive property of the Stokes parameters, the total volume emissivity and Stokes parameters are, respectively, given by $j_i = j_u + j_p$, $dQ_i/ds = dQ_u/ds + dQ_p/ds$ and $dU_i/ds = dU_u/ds + dU_p/ds$.

After collecting all photons from the possible points for each rotation phase Φ and a viewing angle ξ , the degree of the radiation and the position angle of the electric vector of the radiation are, respectively, calculated from $P(\xi, \Phi, \epsilon_1) = \sqrt{Q^2(\xi, \Phi, \epsilon_1) + U^2(\xi, \Phi, \epsilon_1)}/I(\xi, \Phi, \epsilon_1)$

and $\chi(\xi, \Phi, \epsilon_1) = 0.5 \text{atan}[U(\xi, \Phi, \epsilon_1)/Q(\xi, \Phi, \epsilon_1)]$, where $I(\xi, \Phi, \epsilon_1)$, $Q(\xi, \Phi, \epsilon_1)$ and $U(\xi, \Phi, \epsilon_1)$ are the Stokes parameters after collecting photons emitted via both synchrotron radiation and the inverse Compton scattering. The position angle $\chi(\xi, \Phi, \epsilon_1)$ is measured anticlockwise from the axis of the rotation projected on the sky (Figure 11).

3.4. Model parameter

The inclination angle of the pulsars has been constrained by the polarization measurements of the radio pulsed emissions. However, it has not been strongly constrained the inclination angle for the Crab pulsar and PSR B0540-69. Therefore, we treat the inclination angle as a model parameter. The viewing angles ξ of the observer measured from the rotational axis is also a model parameter. For this local model in the magnetosphere, the current should be dealt as a model parameter and the position of the inner boundary depends on the assumed current (Hirotani et al. 2003; Takata et al. 2004, 2006; Hirotani 2006). Instead of the current, however, the ratio of the radial distance to the inner boundary and distance to the the null surface r_n is parameterized and is assumed to be constant for each field line, that is, $r_{in}(\phi)/r_n(\phi)=\text{constant}$, such that the inner boundary locates far away from the stellar surface if the null surface locates far away. For example, from Figure 1, the outer gap accelerator with the non-dimensional current $j \sim 0.22$ has the inner boundary at $r_{in}(\phi)/r_\phi(\phi) \sim 0.65$ in the meridional plane. The altitude of the emission region of the secondary pairs is also model parameter, because the magnetic field will be modified by rotational and plasma effects near the light cylinder and because the last-open field lines may be different from the traditional magnetic file lines that are tangent to the light cylinder in the vacuum case. To specify the upper surface of the outer gap, it is convenient to refer to the footpoint of the magnetic surface on the star and to parameterize the fractional polar angle $a_f = \theta_u/\theta_{lc}$, where θ_u and θ_{lc} are the polar angle of the footpoints of the magnetic surfaces for the gap upper surface and the last-open field line in the vacuum case, respectively. We constrain the boundary of the radial distance to the emission region to $r = R_{lc}$. In this paper, we apply the model to the Crab pulsar in section 4.1 and to a Crab-like pulsar, PSR 0540-69, in section 4.2.

4. Model results

4.1. The Crab pulsar

For the Crab pulsar, we adopt the inclination angle of $\alpha = 50^\circ$, the viewing angle of $\xi = 100^\circ$ and the position of the inner boundary described by $r_{in}(\phi)/r_n(\phi) = 0.67$, which were chosen in Takata et al. (2007). In this paper we chose the fractional angle of $a_f = 1$ to explain the phase-resolved spectra, that is, we assume the gap upper surface with the magnetic field lines that are the conventional last-open field lines in vacuum. The opening angle of the active outer gap in the azimuthal direction is set at $\delta\phi = 250^\circ$, which as assume in section 3.1.

Figure 3 is the photon mapping of the outwardly propagating photons, where the emission direction tangent to the local field lines, which is described by $a_f = 1$, were temporary assumed. Figure 4 shows the variations of the typical radial distance to the emission points of the photons measured by the observer with the viewing angle $\xi = 100^\circ$. The dashed-line in Figure 4 represents the radial distance to the emission points that locate beyond the null surface on the magnetic field lines coming from the north pole. And, the dotted-lines show the distance to the points that locate below the null surface on the magnetic field from the south pole. In the traditional study, only the emission beyond the null surface (dashed-line) have been considered. We will see that the emission component below null surface is required to explain the phase-resolved spectrum of Peak 1 (Figure 8). To calculate the phase-resolved spectra, we define the phase intervals of Peak 1, Bridge, and Peak 2 as $0.06 - 0.16$, $0.29 - 0.4$, and $0.49 - 0.6$ (Figure 4).

4.1.1. Pulse profile and Polarization

Figures 5 and 6 show the predicted variations of the intensity (upper), the position angle of the electric vector of the radiation (middle) and the degree of the polarization (lower) as a function of the pulse phase from optical to γ -ray bands. To compare with the observed pulse profiles in Kuiper et al. (2001), the results were calculated by integrating the photons within the energy interval $1 - 10$ eV, $0.1 - 2.4$ keV, $20 - 100$ keV, $100 - 315$ keV, $0.75 - 10$ MeV and $30 - 100$ MeV. In the figure, we define the rotation phase $\Phi = 0$ in abscissa axis as lying the south pole, and the zero degree in the position angle of the bottom panel is corresponding to the direction of the rotation axis projected on the sky.

In Figures 5 and 6, we see that the calculated pulse profile morphology changes significantly as a function of the photon energy likewise the observational pulse profiles (see figure 5

in Kuiper et al. 2001). One can see in the results that the Peak 1 emissions dominate in the pulse profile in optical bands (left column in Figure 5). But, the intensity ratio of Peak 1 and Peak 2 decreases with increase of the photon energy in optical to soft X-ray bands (middle and right columns in Figure 5), and the ratio becomes unity around 100 keV. Eventually, the Peak 2 emissions dominate the Peak 1 emissions in hard X-ray and soft γ -ray bands as left and middle columns of Figure 6 show. In the hard γ -ray bands, furthermore, Peak 1 again dominates in the pulse profile (right column in Figure 6). This predicted morphology change of the pulse profiles reproduces the observation very well.

With the present outer gap model, the morphology change of the pulse profiles is explained by the radiation properties beyond the null surface, because the major part of the total photons are produced there. The intensity of Peak 1 is much stronger than that of Peak 2 in optical wavelengths, because pileup of the photons emitted from the various positions due to the special relativistic corrections (i.e. the aberration of the emitting direction and the flight-time) occur more efficiently at the Peak 1 phase than the Peak 2 phase. This effect has been considered in the previous studies (Romani & Yadigaroglu 1995; CRZ00) with a constant emissivity. But, the present calculation produces a Peak 2 emission, which becomes more and more pronounced with increasing energies, and eventually dominates the Peak 1 emission in the hard X-ray and the soft γ -ray bands. This is because many photons of Peak 2 are emitted near the stellar surface and on the other hand, most of the photons for Peak 1 are emitted near the light cylinder, as dashed-line in Figure 4 shows. As a result, the phase-resolved spectrum of Peak 2 of the synchrotron photons is harder than that of Peak 1 so that Peak 2 dominates in the pulse profile in hard X-ray and soft γ -ray bands. And finally, the Peak 1 emissions dominate in the hard γ -ray region, where the inverse-Compton process is major emission process (Figure 8). For the inverse Compton scattering with the synchrotron background photons, the averaged strength of the magnetic field affects the power of radiation following equation (4). Because the averaged magnetic field strength in the emission region for Peak 1 is smaller than that for Peak 2, the power of the inverse Compton scattering in the emission region in Peak 1 is larger than that in Peak 2, and as a result Peak 1 dominates in the pulse profile in 30-100 MeV bands. Thus, we find that the synchrotron radiation and inverse Compton scattering of the pairs with the outer gap accelerator model can naturally explain the complex morphology change of the observed pulse profiles.

We see a small peak feature at the leading phase of Peak 1 of the pulse profile of 0.75-10 MeV bands (middle column in Figure 6). We will discuss this feature in section 5 together with the dependency of the results on the model parameters. In fact, this small peak consists of the emissions below the null surface.

For the polarization characteristics, Takata et al. (2007) discussed the predicted characteristics in optical bands (left column in Figure 5) are in general consistent with the observed features (Kanbach et al. 2005) such as a large position angle swing of the electric vector of the radiation at each peak and $\sim 10\%$ of the degree of the polarization between two peaks. In the present study, we find that a similar pattern of the polarization position angle (middle panels of Figures 5 and 6) is predicted in the higher energy bands where the synchrotron process dominates. But, we find that the degree of the polarization in the Bridge emissions depends on the photon energy. As Figure 5 shows, the polarization degree in the Bridge emissions decreases from 10% of the optical wavelengths with increase of the photon energy. This is because the tertiary pairs, which have a small Lorentz factor, contribute to the bridge emissions with about 10 % of the degree of the polarization in the optical wavelengths and contribute with a smaller emissivity in the higher energy region. In 10-100 MeV bands (right column in Figure 6), where the inverse Compton scattering dominates, the degree of the polarization is about 10% is predicted. By comparing the calculated position angles of the Bridge emissions below 1MeV and above 10 MeV, we find that the present model predicts that the observed radiations in 10-100 MeV bands are polarized to the direction orthogonal to the polarization plane of the radiations below 1 MeV.

Above 100 MeV, the attenuated curvature photons from the outer gap explain the observation as we discussed in section 2. Figure 7 summarizes the polarization characteristic of the curvature radiation, where we take into account the acceleration of the particle motion due to the curvature of the field lines and of the co-rotating motion for calculating the polarization characteristic. We assume 80 % of the polarization degree for each radiation. The gyration motion can be ignorable in the outer gap accelerator because the pitch angle of the primary pairs becomes very small $\sin \theta_p \sim 10^{-7}$. We can see from Figure 7 that the intrinsic level of the degree of the polarization at the radiating point is preserved in the Bridge phase for the curvature radiation and a small depolarization appears around the peaks. This less depolarization is because the curvature radiation does not related with the gyration motion of the pairs. This characteristics of the polarization degree of the curvature radiation were also predicted by the caustic model in Dyks et al (2004). The present model predicts that the radiation above 100 MeV of the curvature radiation is highly polarized more than the radiation below 100 MeV of the synchrotron and inverse-Compton process.

4.1.2. Phase-resolved spectra

Figure 8 compares the predicted and observed phase-resolved spectra of the emissions of the Peak 1 (left), Bridge (middle) and Peak 2 (right) phases for the Crab pulsar. The

dashed-line and the dotted-line are, respectively, the spectra of the synchrotron emissions of the secondary pairs beyond and below the null surface. The dashed-dotted line represents the spectrum the inverse Compton scattering and includes the emission both beyond and below null surface, and the dashed-dotted-dotted line represents the appearance curvature spectrum of the primary particles in the gap . The solid-line represents the spectrum of the total emissions. . To compare the results with the data (Kuiper et al. 2001), we normalize the calculated spectrum of Peak 1 to data, but we did not normalize individually on the pulse phase.

From the left panel in Figure 8, we see that the synchrotron emissions below (dotted-line) and beyond (dashed-line) the null charge surface contribute to the total emissions of Peak 1 and Peak 2. Although the flux of the emissions below the null surface is a smaller than that of the emissions beyond the null surface, we find from the figure that the emissions below null surface push up the total flux between 1 MeV and 10 MeV bands for Peak 1 so that the calculated phase-resolved spectrum is in general consistent with the data over the optical to γ -ray bands. If we consider only the emissions beyond the null surface likewise the traditional outer gap model, we obtain calculated total flux of Peak 1 that is significantly smaller than the observed flux between 1 MeV and 10 MeV bands. This is because only emissions around the light cylinder contribute to Peak 1 as the dashed line in Figure 4 shows. Because the typical energy of the synchrotron emissions is below 1 MeV with $B \sim 10^6$ Gauss of the magnetic field around the light cylinder, its flux decreases exponentially above 1 MeV as dashed-line in the left panel of Figure 8 shows. On the other hands, we see that the synchrotron emissions below the null charge surface contribute to the emission above 1 MeV. This is because the emission region below the null surface for Peak 1 spreads from near the stellar surface to near the light cylinder and because the synchrotron emissions with higher magnetic field near the stellar surface contribute to the spectrum.

For Peak 2 (right panel in Figure 8), we find that the observed emissions below 10 MeV are explained by only the synchrotron emissions beyond the null surface, unlike with the Peak 1 emissions. For Peak 2 phase, the radiating points from near the stellar surface to near the light cylinder contribute to the spectrum as the emissions beyond the null surface as Figure 4 shows. Therefore, the spectrum of the synchrotron photons emitted beyond the null charge surface extends above 1 MeV, as dashed line in right panel of Figure 8 shows. The emission region below the null surface locates only near the light cylinder so that the emissions (dotted-line in the right column of Figure 8) is negligible compared with the emissions beyond the null surface.

In the Bridge phase, one can see in Figures 4 and 8 that the photons emitted only beyond the null surface are measured by the observer with the viewing angle $\xi = 100^\circ$. This

is due to the geometry of the dipole magnetic field, and this feature does not depend on the position of the location of the inner boundary, providing that we consider only the outward radiations. Namely, the outward emissions contribute to only the Peak 1, Peak 2 and off-pulse emissions. Therefore, the present model predicts that the Peak 1 and Peak 2 emissions consist of the two components (i.e. emissions below and beyond null surface), while the Bridge emissions consist of only one component (i.e. emissions beyond null surface). This prediction may be consistent with the observational spectral study done by Massaro et al. (2006), who fitted the phase-resolved spectra below 10 MeV with specific two functions for Peak 1 and Pea 2, while one function for Bridge.

When we normalize the model phase-resolved spectra to the observation of Peak 1, we find that the calculated flux of the synchrotron emission in Bridge becomes large compared with the observation as middle panel in Figure 8 shows. We consider that this problem will be related with the three-dimensional structure of the emission region (section 5).

Between 10 MeV and 100 MeV bands, the emissions from the inverse-Compton scattering explain the observation. The present model predicts the flux ratio of 1 MeV emissions and 100 MeV emissions in Bridge phase is larger than those in Peak 1 and Peak 2. This feature is consistent with the observations. With the present synchrotron emission and the inverse-Compton scattering model, the flux ratio of 1 MeV emissions and the 100 MeV emissions is proportional to square of the strength of the magnetic field. The average magnetic field in the emission region for Bridge is larger than those for Peak 1 and Peak 2, because the emission region of Bridge locates nearer the stellar surface than those of the Peak 1 and Peak 2 (Figure 4). As a result, the predicted flux ratio is larger in the Bridge phase than the Peak 1 and Peak 2 phases.

From Figure 8, above 500 MeV bands, the attenuated curvature radiation from the outer gap (dashed-dotted-dotted-line) explains observation.

4.2. PSR B0540-69

PSR B0540-69 is sometimes referred to as a twin of the Crab pulsar. Its rotational period, surface magnetic field, and spin down luminosity are similar to those of the Crab pulsar. Both pulsar have similar spectral features in X-ray bands. The observed flux ratio (< 0.01) of PSR B0540-69 to the Crab pulsar will represent ratio of the distances to the pulsars, which are $d \sim 49$ kpc for PSR B0540-69 and $d \sim 2$ kpc for the Crab pulsar. Furthermore, the radio giant emissions, which may be associate with the high-energy emissions, have been observed from both pulsars (Johnston et al. 2004). While they have theses similarities, the

observed pulse profiles are quite different to each other. The pulse profile of PSR B0540-69 consists of a single broad peak and top of the pulse shape becomes relatively flat, whereas the pulse profile of the Crab pulsar shows a sharp double-peak structure. de Plaa et al (2003) suggested that the observed pulse profile of PSR B0540-69 is result of two pulses separated 0.2 in phase. These difference will be useful to examine the model capability.

The magnetospheric X -ray photon number density will be proportional to $n_x \propto L_{gap}/R_{lc}^2$, where $L_{gap} \sim f(R_{lc}/2)^3 L_{sd}$ and $L_{sd} \sim 3.85 \times 10^{31} P^{-4} B^2$ erg/s is the spin down energy. The ratio of the value of the mean free path, $\lambda \propto 1/n_x$, of a primary curvature photon in the magnetospheres of PSR B0540-69 to the Crab pulsar is estimated as ~ 2 . Because the thickness of the emission region of the secondary pairs is expected to be related with the mean free path of the pair-creation, PSR B0540-69 will have a thicker emission regions of the secondary pairs than the Crab pulsar.

Zhang & Cheng (2000) set the gap thickness of PSR B0540-69 as $\lambda \sim 0.21 R_{lc}$, and they chose the inclination angle $\alpha \sim 50^\circ$ and the viewing angle $\xi = 76^\circ$. The dashed-line in left panel of Figure 9 shows the pulse profile in 10-20 keV bands for the inclination angle $\alpha \sim 50^\circ$ and for the viewing angle $\xi = 76^\circ$ and $\xi = 104^\circ$. The present model produces a broad single peak in the pulse profile as Zhang & Cheng (2000) showed. In this viewing angle, however, we see that the flat feature of the top of the pulse profile appear with a shorter width (~ 0.1 in rotational phase) than the observational value ~ 0.2 . A viewing angle more far from 90° produces a more narrow pulse. On the contrary, if we adopt a closer viewing angle to 90° , the produced pulse profile has two distinct sharp peaks.

With the dipole magnetic field configuration, a more consistent results with the observation is obtained with a smaller inclination angle than $\alpha = 50^\circ$. The solid-line of the left panel in Figure 9 shows the pulse profile of 10-20 keV bands with the inclination angle $\alpha = 30^\circ$ and the viewing angle $\xi = 98.5^\circ$ (and $\xi = 81.5^\circ$). We see that a wider pulse width is produced and the shape of the top of the pulse profile is more similar with the observed profile (see figure 2 of de Plaa et al. 2003). Therefore, the present model predicts that PSR B0540-69 has a thicker emission region (about factor two) than the Crab pulsar and a smaller inclination angle than $\alpha = 50^\circ$.

The expected phase-averaged spectrum in optical to γ -ray bands is displayed in right panel of Figure 9 and is consistent with the observations except for the UV data. Figure 10 shows the calculated pulse profile in the optical bands. We see that the pulse width of the optical bands becomes wider than that of the X-ray bands and the narrower first peak becomes more stronger than the narrower second peak. These features are also consistent with the data. We also display the predicted polarization characteristics in the optical bands for $\xi = 98.5^\circ$ in Figure 10. For the viewing angle $\xi = 81.5^\circ$, which is mutually symmetric

with respect to the rotational equator with $\xi = 98.5^\circ$, the expected pulse profile and the degree of the polarization are identical with those in Figure 10, but the position angle of the polarization is mirror symmetry of that in Figure 10 with respect to the equator 0° .

5. SUMMARY AND DISCUSSION

In summary, we studied non-thermal emission process of the Crab pulsar with the two-dimensional electro-dynamical and the three-dimensional studies. We calculated the synchrotron and the curvature radiation process of the primary particles in the gap using the electro-dynamical study and showed a result which produces a consistent gamma-ray spectrum with EGRET observation. Base on the two-dimensional electro-dynamical study, we conducted the three-dimensional model to calculate the synchrotron and the inverse Compton scattering of the secondary pairs. We computed the pulse profiles, spectra and polarization characteristics in optical to γ -ray bands to compare the data of the Crab pulsar and PSR B0540-69. In the three-dimensional study, we demonstrated that the synchrotron radiation and the inverse Compton scattering with the outer gap geometry naturally explain the morphology change of the observed pulse profiles for the Crab pulsar. We also showed that the observed phase-resolved spectra of the Crab pulsar are explained by the synchrotron radiation and the inverse Compton scattering of the pairs below and beyond the null surface. The predicted polarization characteristics of the Crab pulsar were in general consistent with the data in the optical wavelengths. We also found that a broad single pulse profiles and phase-averaged spectrum of PSR B0540-69 are explained by the present outer gap model with a thicker emission region and a smaller inclination angle than the Crab pulsar.

We have shown that the present outer gap model can explain a lot of the observational properties. But, a further discussion for the emission of soft γ -ray regions will be required, because we found that the calculated pulse profiles of soft γ -ray regions, say 0.75-10 MeV, easily has a triple-peak structure in a single period, as the calculated pulse profile of 0.75-10 MeV in Figure 6 indicates. In this section, therefore, we discuss the pulse profile of the 0.75-10 MeV bands together with the dependency of the results on the model parameters.

As Figure 4 shows, the both emissions beyond and below the null surface contribute to Peak 1. In this case, the small leading peak, which leads the main first peak, easily appears in the pulse profile of 0.75-10 MeV, because the synchrotron spectrum below the null surface is harder than that below the null surface. Below MeV bands, the intensity of the small peak is much weaker than that of the main first peak, and therefore it can not be identified in the pulse profile. However, the emissions beyond null surface, which are major contribution of the Peak 1 emissions, are soft so that the intensity decreases exponentially above 1 MeV as

the calculated phase-resolved spectrum (the dashed line in left panel of the Figure 8) shows. On the other hands, the spectrum of the emissions below the null surface extends above 1 MeV because the photons were emitted near the stellar surface. As a result, the peak by the synchrotron emissions below the null surface becomes conspicuous in the pulse profile above 1 MeV.

With a viewing angle more close to 90° than the present $\xi = 100^\circ$, one can obtain a pulse profile with only two peaks in over the energy bands. In this case, the leading small peak appears the same phase with and are not discriminated from Peak 1 even in the pulse profile of 0.75-10 MeV bands. In such a viewing angle, however, the phase separation between the main two peaks (Peak 1 and Peak 2) is equal to or larger than 0.5 phase. For a viewing angle more far from 90° , on the other hands, the triple-peak structure appears not only in the pulse profile of 0.75-10 MeV bands, but also the pulse profiles in lower energy bands. On these ground, we consider the viewing angle $\xi \sim 100^\circ$ is better fit parameter for the inclination angle of $\alpha = 50^\circ$.

The altitude of the magnetic surface for the lower boundary of the pair emission region (i.e. the upper boundary of the outer gap) also affects to the pulse profile. When we adopt a more higher altitude as the position of the boundary than the present position (i.e. when we adopt a smaller value of $a_f = \theta_u/\theta_{lc}$ than the present $a_f = 1$), the phase separation between the leading small peak and the main first peak becomes wider. As a result, the pulse profiles have three peaks in a single period from optical to γ -ray bands. On the contrary, when we adopt a lower altitude for the position of the boundary with a fraction angle a_f larger than unity, we obtain the pulse profiles having only two main peaks, but the phase separation between two-peaks becomes to be equal to or larger than 0.5 phase. As the lower boundary of the secondary emission region, therefore, we conclude that a magnetic surface close to the surface of the conventional last-opened field lines, $a \sim 1$, is preferred for the lower boundary of the emission region. We also examined the different inclination angle. For example, the inclination angle $\xi = 60^\circ$, the viewing angle $\xi \sim 100^\circ$ and $a_f = 0.99$ reproduced the consistent phase-resolved spectra and the pulse profiles with the Crab data. However, we also obtain a small leading peak in the pulse profile of the 0.75-10 MeV.

Because the phase of the peak in the pulse profile depends on the configuration of the magnetic field, the present results would indicate that the actual magnetic field in the pulsar magnetosphere is modified on important level from the vacuum dipole by plasma effects (Muslimov & Harding 2005). To examined this issue, we need to solve the magnetic field configuration with the current.

A more quantitative arguments in the three-dimensional structure of the magnetosphere will be required to resolve also issue that the calculated Bridge emissions are large relatively

to the observed emissions in the soft γ -ray bands, when we normalize the calculated flux using the Peak 1 emissions, as Figure 8 shows. This will indicate that the dependence of the trans-field thickness of the emission region is described as a more complex function of the azimuth than the present model, in which the emission region was assumed to be located between two magnetic surfaces. In the actual magnetosphere, the trans-field thickness around the meridional plane, where the Bridge emissions take place, may be small relative to the thickness of the leading and the trailing sides, which produce the Peak 1 and Peak 2 emissions. This will be expected because the null charge surface is located nearer the stellar surface around the meridional plane compared with the leading and the trailing side. Therefore, the surface X -rays are more dense around the null surface in the meridional plane so that the mean-free path of the pair-creation and the resultant trans-field thickness of the outer gap and the emission regions are shorter around the meridional plane than that of the leading and trailing sides. Since the three-dimensional structures of the acceleration region and the emission region have not been solved up to now, the above issues will demand us to perform a more quantitatively study of the three-dimensional structure in the subsequent papers.

Finally, we note that it is important to observationally constrain the inclination angle. Takata et al. (2007) searched the parameter range to explain the polarization characteristics and the pulse profile in the optical wavelengths of the Crab pulsar. In their study, a wide range of the viewing angle for each inclination angle was allowed for the possible parameters to explain the optical pulse profile and the polarization. In this study, we found that the narrower range of the viewing angle can produce the consistent pulse profile and phase-resolved spectra with data in optical to γ -ray bands. Therefore, if the inclination angle can be determined in other ways, the viewing angle will be strongly constrained by the present study.

Authors appreciate fruitful discussion with K.S. Cheng, K.Hirotsu, S.Shibata and R.Taam. Authors also thank anomarous referee for insightful comments on the manuscript. This work was supported by the Theoretical Institute for Advanced Research in Astrophysics (TIARA) operated under Academia Sinica and the National Science Council Excellence Projects program in Taiwan administered through grant number NSC 96-2752-M-007-001-PAE.

A. Stokes parameter of the inverse Compton scattering

In this appendix, we derive the Stokes parameters given by equations (8) and (10), which are respectively the Stokes parameters of the inverse Compton process for the unpolarized

and the polarized background radiation.

In this appendix, as polar-axis (z-axis), we choose the direction of the particle motion at local point. With equation (3), the unit vector \mathbf{e}_z^* along the z-axis is described by the unit vectors (without asterisk) in the coordinate system based on the rotation axis as

$$\mathbf{e}_z^* = \beta_0 \cos \theta_p \mathbf{b} + \beta_0 \sin \theta_p \mathbf{b}_\perp + \beta_{co} \mathbf{e}_\phi, \quad (\text{A1})$$

where θ_p is the pitch angle, \mathbf{b} is the unit vector along the magnetic field, and $\mathbf{b}_\perp = \pm(\cos \delta\phi \mathbf{K} + \sin \delta\phi \mathbf{K} \times \mathbf{b})$ is the unit vector perpendicular to the magnetic field line, \mathbf{K} is the unit vector of the curvature of the magnetic field, and $\delta\phi$ is the phase of the gyration motion. The parameter β_0 is determined from $|\mathbf{e}_z^*| = 1$. We define x and y axes with (Figure 11)

$$\mathbf{e}_x^* = [\beta_0 \mathbf{K} - (\beta_c K_\phi / b_r) \mathbf{e}_r] / |[\beta_0 \mathbf{K} - (\beta_c K_\phi / b_r) \mathbf{e}_r]|, \quad \text{and} \quad \mathbf{e}_y^* = \mathbf{e}_z^* \times \mathbf{e}_x^* \quad (\text{A2})$$

The propagating direction of the background radiation, \mathbf{k}_0 , are represented by a polar angle θ_0 and a azimuthal angle ϕ_0 , that is, $\mathbf{k}_0 = \sin \theta_0 \cos \phi_0 \mathbf{e}_x^* + \sin \theta_0 \sin \phi_0 \mathbf{e}_y^* + \cos \theta_0 \mathbf{e}_z^*$. The propagating direction of the scattered radiation, \mathbf{k}_1 , is represented by coordinates (θ_1, ϕ_1) . If a particle moves with the Lorentz factor Γ_e , we relate the quantities of the rest frame of the electron (with prime) and of the observer frame (without prim) as

$$\cos \theta' = (\cos \theta - \beta) / (1 - \beta \cos \theta), \quad \phi' = \phi,$$

for the polar and azimuthal angles and $\epsilon = \Gamma(1 + \beta \cos \theta') \epsilon'$ for the photon energy. If the background radiation is polarized, we describe the direction of the polarization with $\mathbf{E}_w = \sin \theta_w \cos \phi_w \mathbf{e}_x^* + \sin \theta_w \sin \phi_w \mathbf{e}_y^* + \cos \theta_w \mathbf{e}_z^*$.

In the calculation, we first compute the Stokes parameters of the Compton process in the electron rest frame, and then we perform the Lorentz transformation to the observer frame.

A.1. Unpolarized background field

For the Compton scattering with the unpolarized background radiation, the Stokes parameters, which are represented in the coordinate basis orthogonal to and parallel to the scattering plane, in the electron rest frame are

$$\left. \begin{array}{l} s_0^{u'} \\ p_\perp^{u'} \\ p_\parallel^{u'} \end{array} \right\} = \left\{ \begin{array}{l} \left[\frac{\epsilon'_0}{\epsilon'_1} + \frac{\epsilon'_1}{\epsilon'_0} - \sin^2 w'_s \right] \\ \sin^2 w'_s \\ 0 \end{array} \right. \quad (\text{A3})$$

(McMaster, 1961), where $s_0^{u'}$ corresponds to the emissivity, $p_{\perp}^{u'}$ and $p_{\parallel}^{u'}$ describe the polarization direction orthogonal to and the parallel to the plane of the scattering, respectively. The dimensionless quantities ϵ'_0 and ϵ'_1 are, respectively, the energy of the background and the scattered photons in units of the electron rest mass energy and are connected by $\epsilon'_1 = \epsilon'_0/[1 + \epsilon'_0(1 - \cos w'_s)]$. The scattering angle w'_s is defined by

$$\cos w'_s = \mathbf{k}'_0 \cdot \mathbf{k}'_1 = \sin \theta'_0 \sin \theta'_1 \cos(\phi_0 - \phi_1) + \cos \theta'_0 \cos \theta'_1. \quad (\text{A4})$$

For the unpolarized background radiation, we find that the scattered radiation is partially polarized orthogonal to the scattering plane.

We transform the back ground frame to the one related with the particle motion direction (z-axis) projected onto the sky. Using such coordinate system, the Stokes parameters become

$$q'_u = p_{\perp}^{u'} \cos 2\eta' - p_{\parallel}^{u'} \sin 2\eta' = \sin^2 w'_s \cos 2\eta', \quad (\text{A5})$$

and

$$u'_u = p_{\perp}^{u'} \sin 2\eta' + p_{\parallel}^{u'} \cos 2\eta' = \sin^2 w'_s \sin 2\eta', \quad (\text{A6})$$

where η' is angle between the projected z-axis on the sky and the direction orthogonal to the scattering plane, and its cosine is given by $\cos \eta' = -\sin \theta'_0 \sin(\phi'_0 - \phi'_1)/\sin w'_s$ (Figure 11).

Writing the unpolarized background radiation in the rest frame with $I_b^u(\epsilon_0, \mathbf{k}'_0)$, the Stokes parameters of the total amount of the scattered radiation are give by $i^{u'}(\epsilon'_1, \mathbf{k}'_1) = (3\sigma_T/16\pi) \int I_b^{u'} s_0^{u'} d\Omega'$, $Q'_u(\epsilon'_1, \mathbf{k}'_1) = (3\sigma_T/16\pi) \int I_b^{u'} q'_u d\Omega'$, and $U'_u(\epsilon'_1, \mathbf{k}'_1) = (3\sigma_T/16\pi) \int I_b^{u'} u'_u d\Omega'$, respectively. If we take the Thomson limit, $\epsilon'_0 = \epsilon'_1$, we arrive the equations (2), (4a) and (4b) of Begelman and Sikora (1987).

By performing the Lorentz transformation from the electron rest frame to observer inertial frame, and by transforming the background coordinate to one related the projected rotation axis on the sky, the Stokes parameters become

$$\begin{aligned} i(\mathbf{k}_1, \epsilon_1) &= D_2^3 i^3(\mathbf{k}'_1, \epsilon_1) \\ q(\mathbf{k}_1, \epsilon_1) &= D_2^3 [q'(\mathbf{k}'_1, \epsilon'_1) \cos 2\zeta - u'(\mathbf{k}'_1, \epsilon'_1) \sin 2\zeta], \\ u(\mathbf{k}_1, \epsilon_1) &= D_2^3 [u'(\mathbf{k}'_1, \epsilon'_1) \cos 2\zeta + q'(\mathbf{k}'_1, \epsilon'_1) \sin 2\zeta], \end{aligned} \quad (\text{A7})$$

where $D_2 = \epsilon_1/\epsilon'_1 = \Gamma_e^{-1}(1 - \beta \cos \theta_0)^{-1}$ is the Doppler factor, and the azimuth angle ζ is defined by angle between the angle between the direction of the rotation axis and of the particle motion projected on the sky.

Finally, integrating i , q and u over the particle momentum distribution, the Stokes

parameters are given by

$$\left. \begin{aligned} dI_u(\mathbf{k}_1, \epsilon_1)/ds \\ dQ_u(\mathbf{k}_1, \epsilon_1)/ds \\ dU_u(\mathbf{k}_1, \epsilon_1)/ds \end{aligned} \right\} = \int d\Gamma_e \left[\frac{dn_e}{d\Gamma_e} \right] (1 - \beta \cos \theta_0) \times \begin{cases} i(\mathbf{k}_1, \epsilon_1), \\ q(\mathbf{k}_1, \epsilon_1), \\ u(\mathbf{k}_1, \epsilon_1), \end{cases} \quad (\text{A8})$$

where the extra factor $(1 - \beta \cos \theta_0)$ represents relative motion of photons and particles along the photon motion.

Now, we suppose the total background radiation in the observer frame that $I_b(\mathbf{k}_0, \epsilon_0) = C_0 \epsilon_0^{-\alpha} \delta(\theta - \theta_0) \delta(\phi - \phi_0)$. In the rest frame of an electron, the background radiation distributes as

$$I'_b(\mathbf{k}'_0, \epsilon'_0) = D_1^3 I_b(\mathbf{k}_0, \epsilon_0) = \frac{C_0 \epsilon_0'^{-\alpha}}{\Gamma_e^{1+\alpha} (1 + \beta \cos \theta')^{1+\alpha}} \delta(\theta' - \theta'_0) \delta(\phi' - \phi'_0), \quad (\text{A9})$$

where we use $D_1 = \epsilon'_0/\epsilon_0 = \Gamma_e^{-1} (1 + \beta \cos \theta')^{-1}$, and $\delta(\theta - \theta_0) \delta(\phi - \phi_0) = D_1^{-2} \delta(\theta' - \theta'_0) \delta(\phi' - \phi'_0)$, which is because $\delta(\theta - \theta_0) \delta(\phi - \phi_0) d\Omega = \delta(\theta' - \theta'_0) \delta(\phi' - \phi'_0) d\Omega'$ and $d\Omega = D_1^2 d\Omega'$.

By denoting the polarization degree of the total background radiation as Π_{syn} , that is, $I_b^{u'} = (1 - \Pi_{syn}) I'_b$, finally we arrive equation (8),

$$\left. \begin{aligned} dI_u(\mathbf{k}_1, \epsilon_1)/ds \\ dQ_u(\mathbf{k}_1, \epsilon_1)/ds \\ dU_u(\mathbf{k}_1, \epsilon_1)/ds \end{aligned} \right\} = (1 - \Pi) \frac{3\sigma_T}{16\pi} C_0 \int d\Gamma_e \left[\frac{dn_e}{d\Gamma_e} \right] \frac{\epsilon_0^{-\alpha}}{\Gamma_e^{4+\alpha} (1 - \beta \cos \theta_1)^2 (1 + \beta \cos \theta'_0)^{1+\alpha}} \times \begin{cases} s_0^{u'}(\mathbf{k}'_1, \epsilon'_1), \\ q'_u(\mathbf{k}'_1, \epsilon'_1) \cos 2\zeta - u'_u(\mathbf{k}_1, \epsilon_1) \sin 2\zeta, \\ q'_u(\mathbf{k}'_1, \epsilon'_1) \sin 2\zeta + u'_u(\mathbf{k}_1, \epsilon_1) \cos 2\zeta. \end{cases} \quad (\text{A10})$$

A.2. Polarized background field

For the polarization background radiation, the Stokes parameters corresponding to equation (A3) become

$$\left. \begin{aligned} s_0^{p'} \\ p_{\perp}^{p'} \\ p_{\parallel}^{p'} \end{aligned} \right\} = \begin{cases} \left[\frac{\epsilon'_0}{\epsilon'_1} + \frac{\epsilon'_1}{\epsilon'_0} - \sin^2 \theta'_1 \cos^2 \lambda'_p \right] \\ \sin^2 \theta'_1 - (1 + \cos^2 \theta'_1) \cos 2\lambda'_p \\ 2 \cos \theta'_1 \sin 2\lambda'_p \end{cases} \quad (\text{A11})$$

where λ'_p is the angle between the polarization plane of the background radiation and the orthogonal plane to the scattering plane and its cosine is given by

$$\begin{aligned} \cos \lambda'_p &= (\sin w'_s)^{-1} [\sin \theta'_0 \cos \theta'_1 \sin \theta'_w \sin(\phi_0 - \phi_w) + \cos \theta'_0 \sin \theta'_1 \sin \theta'_w \sin(\phi_w - \phi_1) \\ &+ \sin \theta'_0 \sin \theta'_1 \cos \theta'_w \sin(\phi_1 - \phi_0)], \end{aligned} \quad (\text{A12})$$

where θ'_w and ϕ'_w represent the polar angle and the azimuthal angle of the polarization plane of the background radiation, respectively.

Transforming the background coordinate to one related with the particle motion, the components of the Stokes parameters representing the polarization are, respectively, given by

$$q'_p = [\sin^2 w'_1 - (1 + \cos^2 w') \cos 2\lambda'_p] \cos 2\eta' - 2 \cos' w \sin 2\lambda'_p \sin 2\eta, \quad (\text{A13})$$

and

$$u'_p = [\sin^2 w'_1 - (1 + \cos^2 w') \cos 2\lambda'_p] \sin 2\eta' + 2 \cos' w \sin 2\lambda'_p \cos 2\eta. \quad (\text{A14})$$

After same procedure with the case of the unpolarized background radiation (or replacing subscript u and $1 - \Pi_{syn}$ in the equation (A10) to p and to Π_{syn}), we arrive equation (10).

REFERENCES

- Begelman, M.C., & Sikora M. 1987, ApJ, 322, 650
- Blaskiewicz, M., Cordes, J.M. & Wasserman, I. 1991, ApJ, 370, 643
- Chang, H.-K., Boggs, S. & Chang, Y.-H. 2007, Adv. Space Res., in press
- Cheng, K.S., Ho, C. & Ruderman, M. 1986a, ApJ, 300, 500
- Cheng, K.S., Ho, C. & Ruderman, M. 1986b, ApJ, 300, 522
- Cheng, K.S., Ruderman, M. & Zhang, L. 2000, ApJ, 537, 964 (CRZ00)
- Daugherty, J.K. & Harding, A.K. 1996, ApJ, 458, 278
- de Plaa, J., Kuiper, L. & Hermsen, W. 2003 A&A, 400, 1013
- Dyks J., Harding A.K. & Rudak B. 2004, ApJ, 606, 1125
- Goldreich, P. & Julian, W.H. 1969, ApJ, 157, 869
- Hirovani, K. 2006, ApJ, 652, 1475
- Jia, J.J., Tang, P.S. Anisia, Takata, J., Chang, H.-K. & Cheng K.S., 2007, Adv. Space Res., in press
- Johnston, S, Romani, R.W., Marshall, F.E.& Zhang, W. 2004, MNRAS, 355, 31

- Kanbach, G., Słowikoska, A., Kellner, S. & Steinle, H. 2005, AIP Conference Proceeding, 801, 306
- Kataoka, J. et al. 2005, Proceedings of the SPIE, 5898, 133
- Kuiper, L., Hermsen, W., Cusumano, G., Diehl, R., Schönfelder, V., Strong, A., Bennett, K. & McConnell, M. L. 2001, A&A, 378, 918
- Massaro, E., Campana, R., Cusumano, G. & Mineo, T. 2006, A& A, 459, 859
- McMaster, W.H. 1961, REv. Mod. Phys., 33, 8
- Mignami, R.P., Bagnulo, S., Dyks, J., Curto, G.Lo & Słowikowska A. 2007, astro-ph/0702307
- Muslimov, A.G. & Harding, A.K. 2004, ApJ, 606, 1143
- Muslimov, A.G. & Harding, A.K. 2005, ApJ, 630, 454
- Romani R.W. 1996, ApJ, 470, 469
- Romani, R.W. & Yadigaroglu, I.-A. 1995, ApJ, 438, 314
- Ruderman, M.A. & Sutherland, P.G. 1975, ApJ, 196, 51
- Scharlemann, E.T., Arons, J. & Fawley, W.M. 1978, ApJ, 222, 297
- Takata, J., Shibata, S. & Hirotani K. 2004, MNRAS, 354, 1120
- Takata, J., Shibata, S., Hirotani, K. & Chang, H.-K. 2006, MNRAS, 366, 1310
- Takata, J., Chang, H.-K., & Cheng, K.S. 2007, ApJ, 656, 1044
- Thompson, D.J. 2003, To appear in Cosmic Gamma Ray Sources, Kluwer ASSL Series, Edited by K.S. Cheng and G.E. Romero (astro-ph/0312272v1)
- Yakovlev, D.G. & Pethick, C.J. 2004, ARA&A, 42, 169
- Zhang, L. & Cheng K.S. 1997, ApJ, 487, 370
- Zhang, L. & Cheng, K.S. 2000, A&A, 363, 575
- Zhang, L. & Cheng, K.S. 2002, ApJ, 569, 872

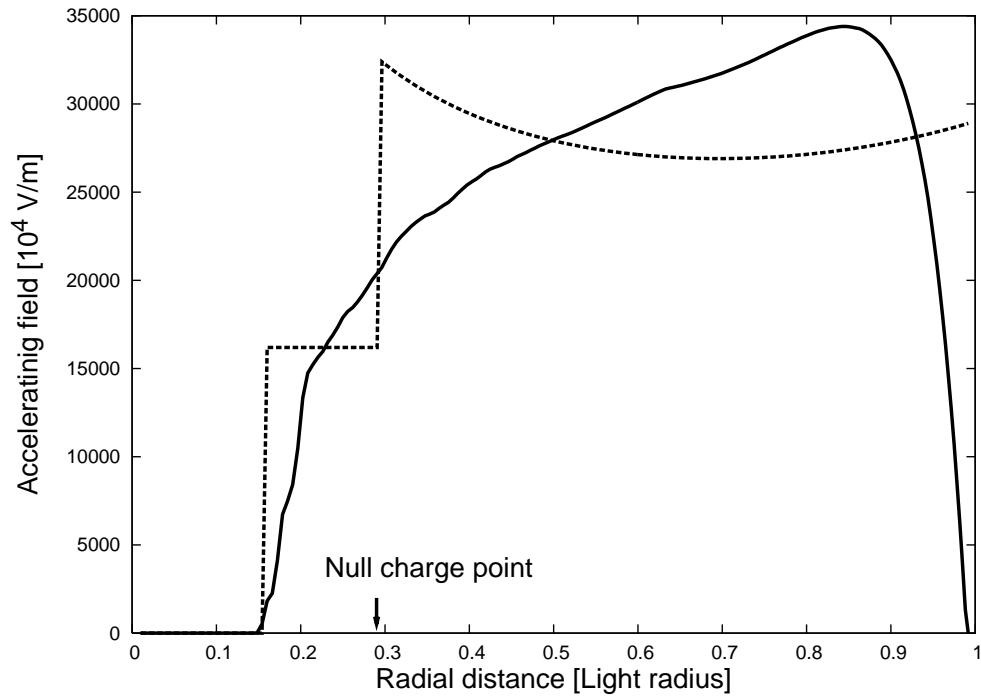


Fig. 1.— Electric structure in the gap. The solid line shows the solved accelerating field along the field line, which locate at 50 % of the thickness from the last open field line. This results are for The inclination angle is 50° and for about 22 % of the Goldreich-Julian current in the gap. Beyond the null charge point, the dashed line is vacuum electric field obtained by Cheng et al (1986a).

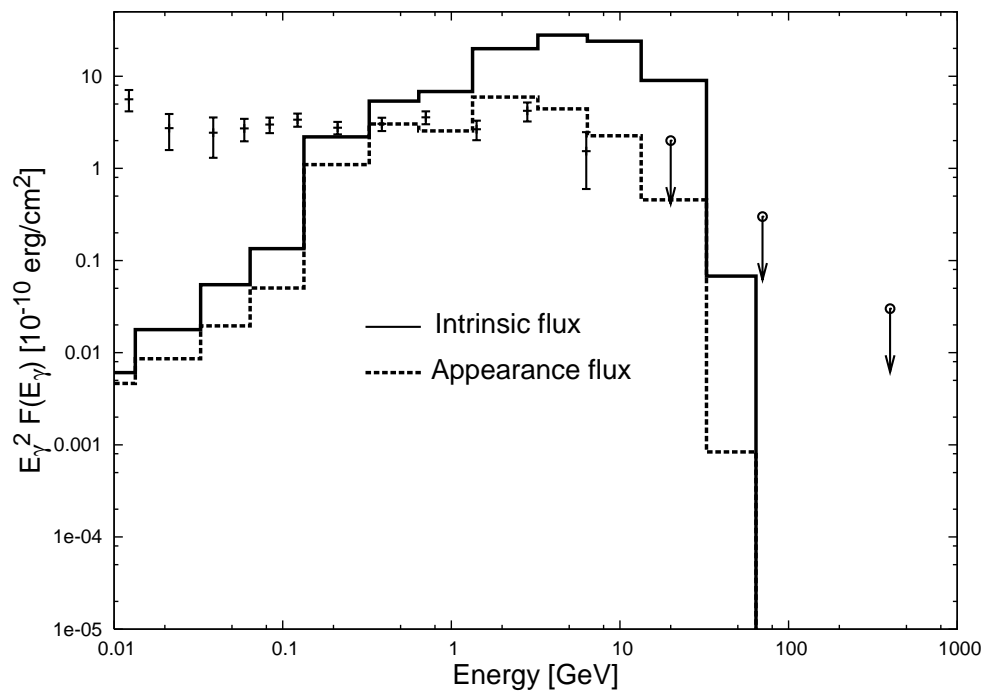


Fig. 2.— The spectrum of the synchrotron and the curvature processes of the primary particles in the outer gap. The solid line represent the intrinsic flux from the outer gap. The dashed line show the appearance flux after pair-creation process outside of the outer gap with the soft photons emitted by the synchrotron radiation of the secondary pairs. The observation data are taken from Kuiper et al. (2002) and reference therein.

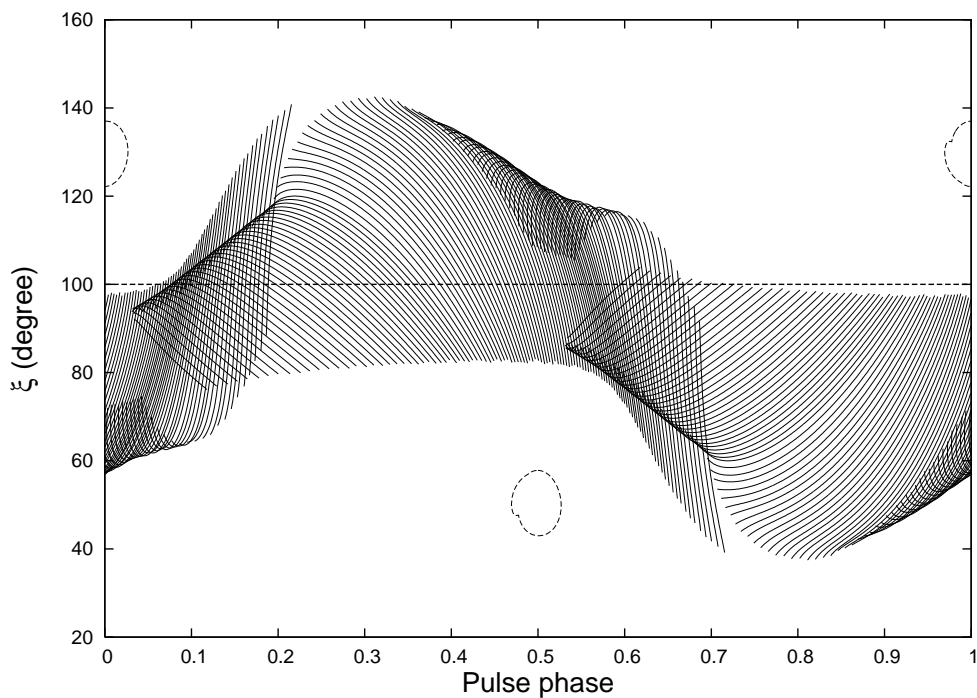


Fig. 3.— Emission region projected onto the (ξ, Φ) -plane for the magnetic surface $a_f = 1$. Here, the emission direction is tangent to the direction of the local magnetic field. The inclination angle is $\alpha = 50^\circ$, the emission region extends from $r_{in} = 0.67$ to $r = R_{lc}$, and the width of the polar cap angle is about 250° . The circles show the shape of the polar cap. The viewing angle $\xi = 100^\circ$ (horizontal dashed-line) is used in the calculations for Figure 4~ 8.

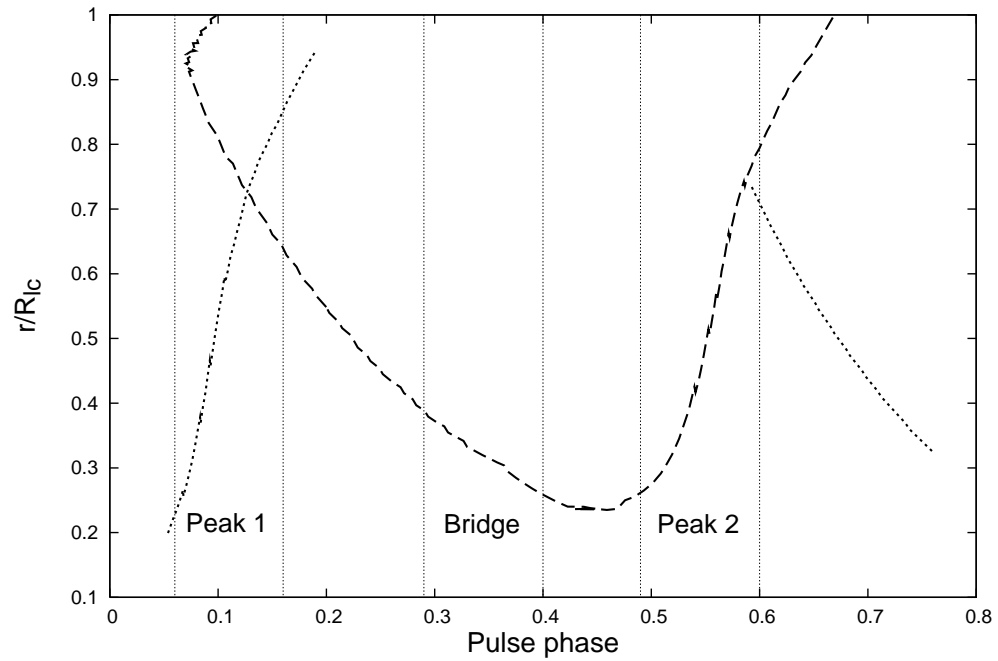


Fig. 4.— Variation of radial distance with pulse phase for the inclination angle $\alpha = 50^\circ$ and the viewing angle $\xi = 100^\circ$. The dashed-line and the dotted-line represent the emission regions beyond and below the null surface, respectively.

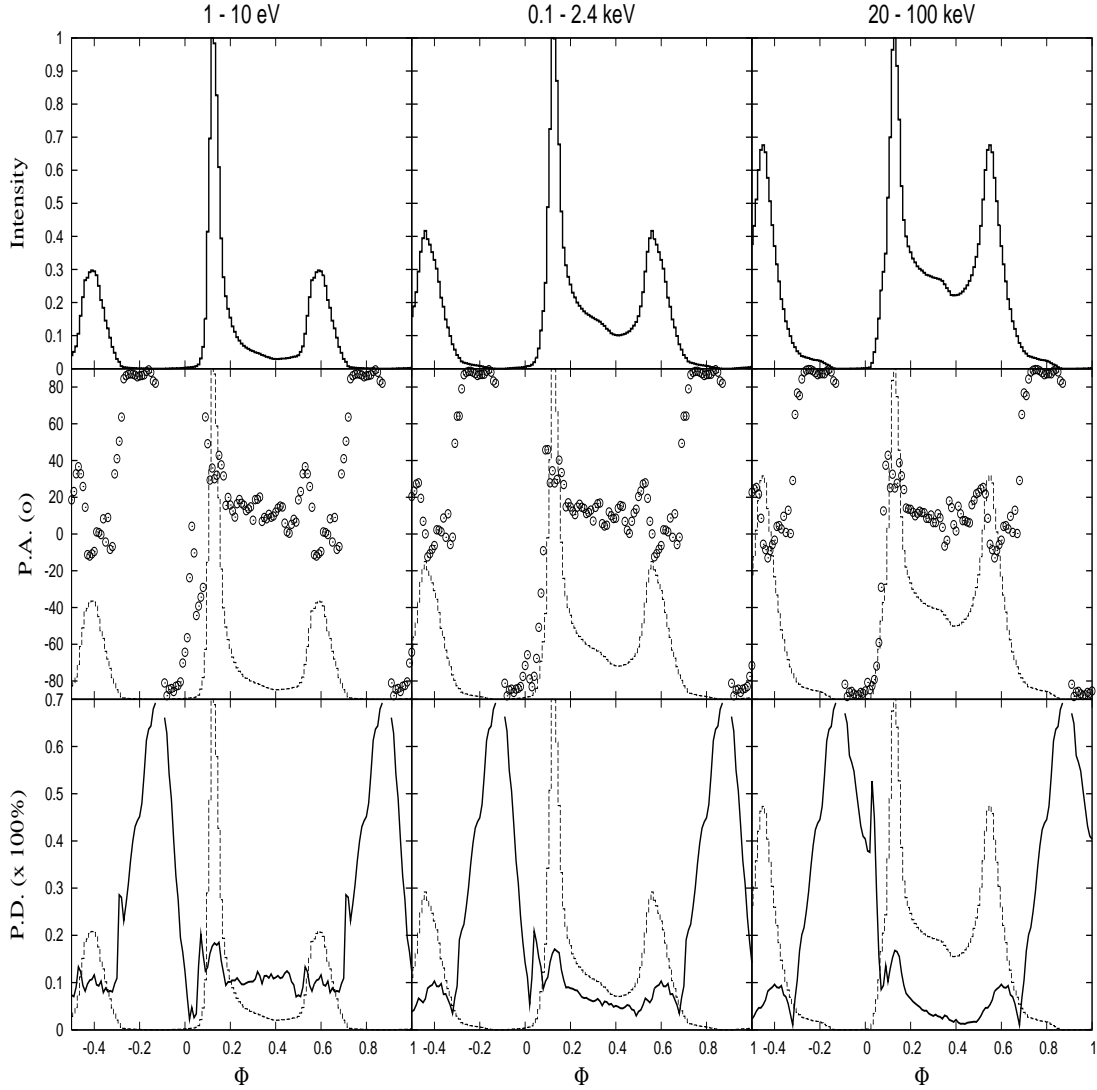


Fig. 5.— Variation of the intensity (tot), the position angle (middle dots) and the degree of the polarization (bottom solid-line) as a function of the rotational phase. For the reference, the light curve is overplotted at middle and bottom panels (thin dashed-lines). To compare with the observe pulse profiles of Kuiper et al. (2001), the results were obtained by integrating the photons within the energy interval 1 – 10 eV (left column), 0.1 – 2.4 keV (middle column) and 20 – 100 keV (right column). The model parameters are $\alpha = 50^\circ$, $\xi = 100^\circ$, $r_{in} = 0.67r_n$ and $a_f = 1$.

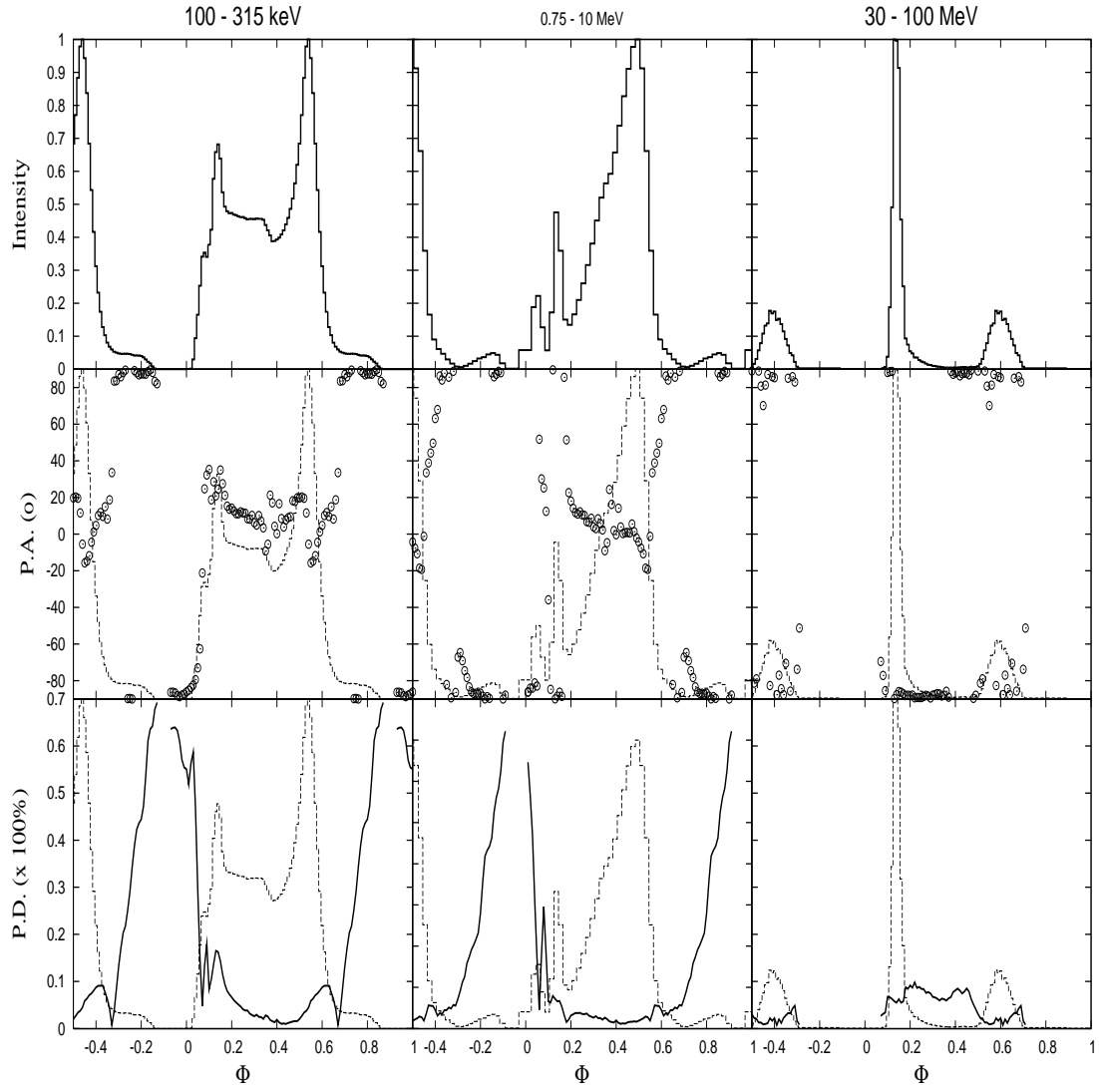


Fig. 6.— Same with the Figure 5, but the results are for the interval of photons energy, 100-315 keV (left), 0.75-10 MeV (middle) and 30-100 MeV (right)

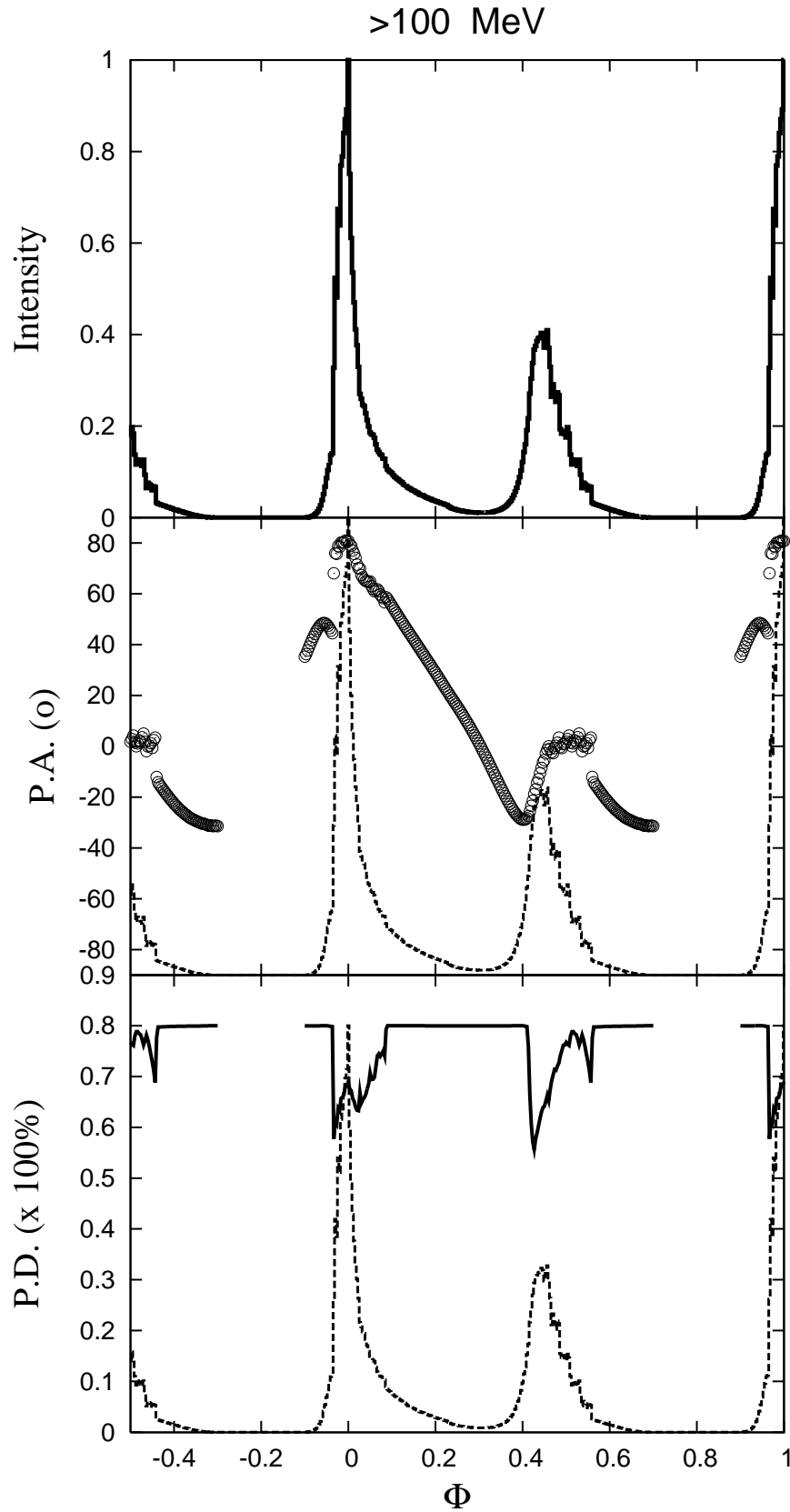


Fig. 7.— The polarization characteristic of the curvature radiation in the outer gap. The 80% of the polarization degree for each radiation was assumed as the intrinsic level. The

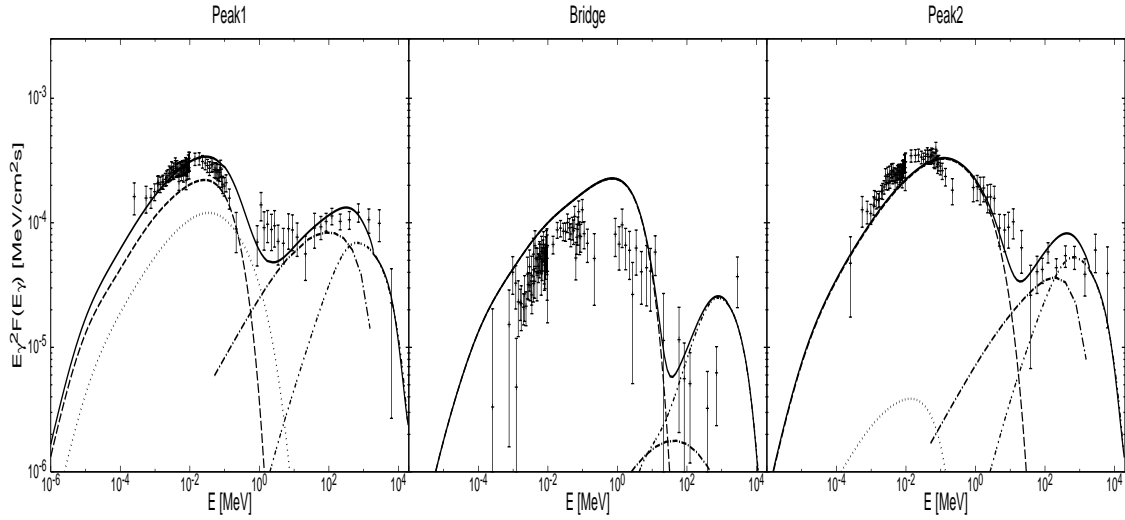


Fig. 8.— Phase-resolved spectra for Peak 1 (left), Bridge (middle) and Peak 2 (right) for the Crab pulsar. The dashed-line and the dotted-line show the spectra of the synchrotron emissions of the pairs beyond and below the null surface, respectively, the dashed-dotted-line show the spectrum of the inverse Compton scattering, and the dashed-dotted-dotted-line show the attenuated curvature spectrum in the outer gap. The solid-line represents the spectrum of the total emissions. The model parameters are $\alpha = 50^\circ$, $\xi = 100^\circ$, $r_{in} = 0.67r_n$ and $a_f = 1$. The observation data are taken from Kuiper et al. (2001).

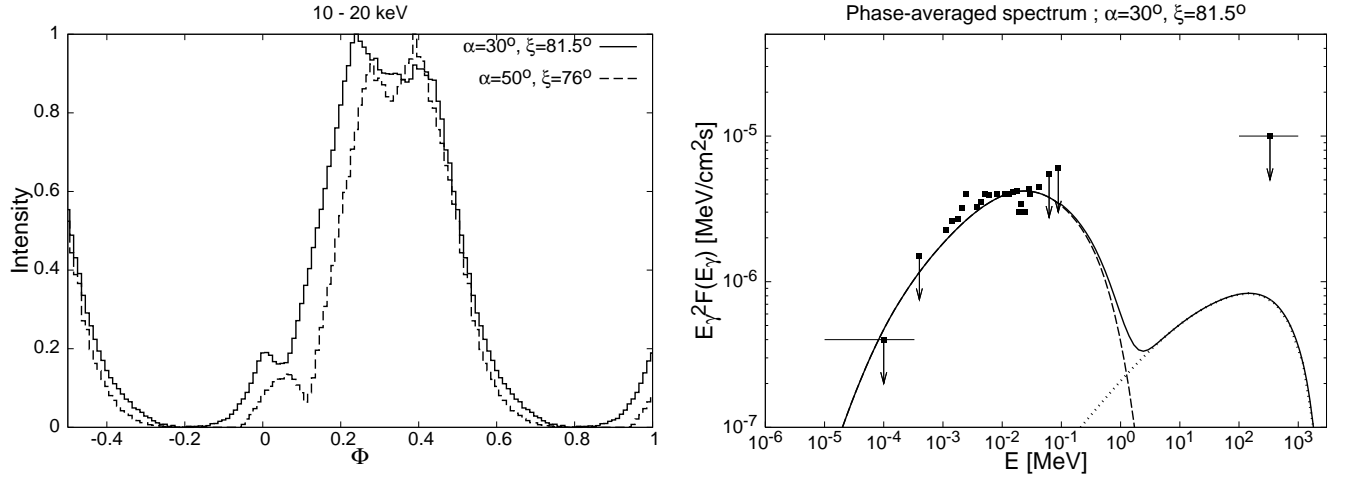


Fig. 9.— Left; The pulse profile in 10-20 keV bands for PSR B0540-69. The solid-line is result for $\alpha = 30^\circ$ and $\xi = 98.5^\circ$ (and $\xi = 81.5^\circ$), and the dashed-line is for $\alpha = 50^\circ$ and $\xi = 104^\circ$ (and $\xi = 76^\circ$). Right; The phase-averaged spectrum of PSR B0540-69 for $\alpha = 30^\circ$ and $\xi = 98.5^\circ$ (and $\xi = 81.5^\circ$). The solid-line represents the total emissions of the synchrotron radiation (dotted-line) and the inverse-Compton scattering (dotted-line). The observation data are take from de Plaa et al (2003).

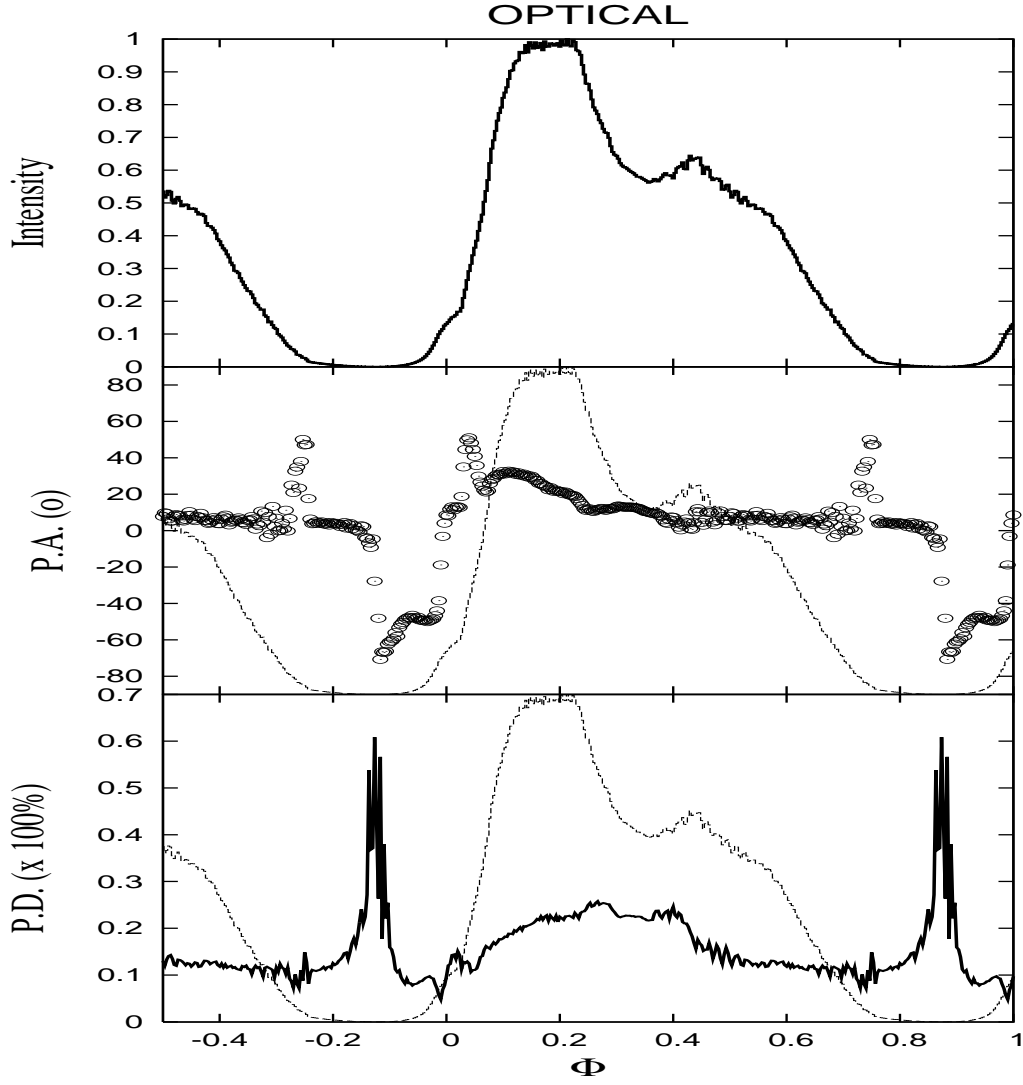


Fig. 10.— Pulse profile in optical bands of PSR B0540-69. The result is for $\alpha = 30^\circ$ and $\xi = 98.5^\circ$. The top, middle and bottom panels show the intensity, the position angle of the polarization and the degree of the polarization, respectively.

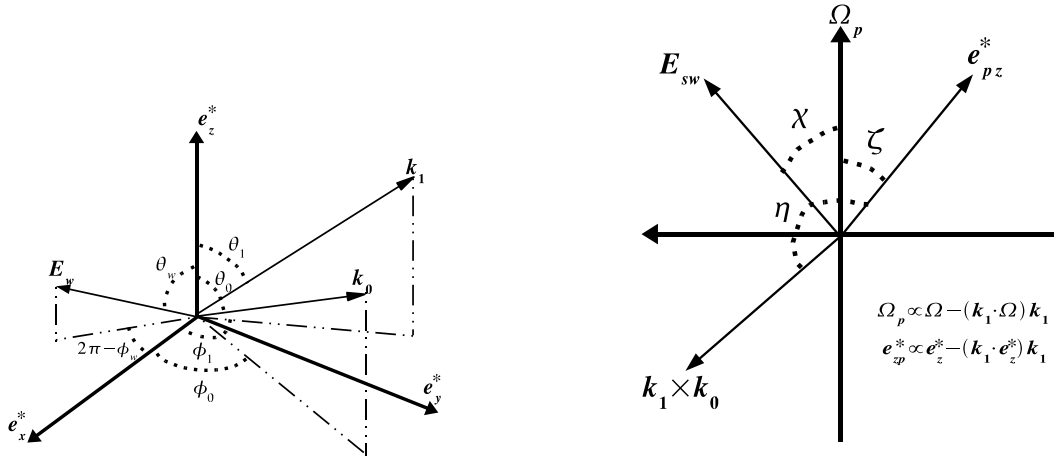


Fig. 11.— Left: Coordinate system used to describe scattering in the electron rest frame. The polar axis, \mathbf{e}_z^* , is chosen to coincide with direction of the electron motion in the observer frame. The definition of \mathbf{e}_x^* and \mathbf{e}_z^* are seen in equation (A2). The vectors \mathbf{k}_0 and \mathbf{k}_1 are the directions of the background and the scattered radiations, respectively. If the background radiation is polarized, the vector \mathbf{E}_w is used to represent the polarization plane of it. Right: Coordinate system on the sky. Ω_p and \mathbf{e}_{zp}^* is, respectively, the directions of the rotational axis and of the particle motion projected on the sky. The position angle of the polarization plane (\mathbf{E}_{sw}) is measured anticlockwise from the direction of the rotational axis on the sky.